35th Symposium on Naval Hydrodynamics
Nantes, France, 8 – 12 July, 2024

4DPTV Measurements and DES of the Turbulence Structure and Vortex Breakdown and Interaction for 5415 Sonar Dome Vortices

F. Stern,[1] Y. Sanada,[1] Z. Starman,[1] S. Bhushan,[2] C. Milano,[1]
([1]IIHR, University of Iowa, USA, [2]Mississippi State University, USA)

ABSTRACT

Additional analyses of the Four-dimensional particle tracking velocimetry (4DPTV) static drift β = 10 deg results for the 5415 sonar dome vortices have been done to realize its full potential for the assessment of the turbulence structure and vortex breakdown and interactions and for providing data for scale resolved computational fluid dynamics (CFD) validation. The 4DPTV has a significantly larger measurement volume size and sampling rate compared to the previous tomographic particle image velocimetry (TPIV), but it has less spatial resolution. The focus is on the strongest primary sonar dome vortex (SDVP) at x/*L* = 0.12 (just downstream of the sonar dome) and its interaction with the second strongest (SDVS) of the multiple sonar dome vortices. Both vortices are counterclockwise and due to cross flow separations with SDVP and SDVS onset from the windward (port) and leeward (starboard) sides of the sonar dome. The macro-scale analysis showed agreement between 4DPTV and TPIV for the SDVP elliptically shaped cross plane streamlines and Gaussian and Bell distribution for the Q-criteria and axial vorticity. The macro-scale turbulence is stronger for the 4DPTV compared to the TPIV, whereas the vortex strength has the opposite trend, and the anisotropy shows both similarities and differences. The detached eddy simulation (DES) shows similar trends as the experiments, but there are large quantitative differences. The micro-scale analysis used model spectrums based on the 4DPTV and TPIV macro-scales as benchmarks, which were about half the size of their spatial resolutions and indicate that sub-millimeter resolution is needed to accurately resolve the micro-scales. The temporal and spatial autocorrelation functions were used to compute micro-scale results. The Taylor micro-scales (λ_f) were consistently larger than their benchmarks and roughly twice their spatial resolutions. The larger λ_f resulted in significantly smaller dissipation ε than the benchmark. The Kolmogorov length scale η values were also larger than the benchmark, but the differences with the benchmark were not as large as that for the λ_f. The temporal 4DPTV analysis resolved the energy containing range and a large portion of the inertial sub-range of the turbulence. The spatial 4DPTV analysis resolved a narrower band compared to the temporal analysis, and primarily resolved the inertial subrange. The anisotropy analysis of the 4DPTV, TPIV, and DES highlights their strengths and limitations for characterizing the turbulence structure. The DES predicts an almost 2D turbulence state whereas the 4DPTV and TPIV display Reynolds stress ellipsoids that resemble oblate and prolate spheroids, respectively. The analysis of the Reynolds stress ellipsoids suggests that the principal axes are largely affected by the differences in the normal components of the Reynolds stresses; however, sensitivity analysis is needed to confirm this postulation. The 4DPTV measurements and DES provide strong evidence that SDVP undergoes a spiral vortex breakdown/helical mode instability like KVLCC2 and 5415 at static drift β = 30 and 20 deg, respectively, and delta wings. The SDVS vortex is shed periodically with visually evident interactions between SDVP and SDVS, which suggests that such vortex interactions induce the SDVP spiral vortex breakdown/helical mode instability at smaller swirl number than what is observed for other flows without such interactions.

INTRODUCTION

The physics, measurement, and prediction of 3D vortex onset and progression, including turbulence structure and vortex breakdown and interactions remains an ongoing fluid dynamics challenge, as evidenced for ship hydrodynamics by the CFD Workshop T2015 (Hino et al., 2020), NATO Working Group AVT-253 (NATO STO, 2021), and the Workshop on Verification and Validation of Ship Maneuvering Simulation Methods (https://www.simman2020.kr/). Recently, Sanada et al. (2023) made significant progress on the physics of the 3D vortex onset and progression for the 5415 sonar dome vortices for straight ahead, static drift β = 10 deg, and pure sway β_{max} = 10 deg via 4DPTV measurements due to its significantly larger

measurement volume and data rate in comparison to the previous TPIV measurements (Yoon and Stern, 2017; Bhushan et al., 2019 and 2021).

The objective of the present research is the additional analysis of the 4DPTV static drift $\beta = 10$ deg results to realize its full potential for the assessment of (1) the turbulence structure and vortex breakdown and interactions and for (2) providing data for scale resolved CFD validation. Another objective (3) is to identify its limitations for future advancements in instrumentation. The approach includes the macro features and large scales, spectral analysis and small scales, turbulence anisotropy, vortex breakdown and interactions, and conclusions and future research, including the additional analysis of not only the 4DPTV data but also the previous TPIV and DES.

Figure 1 (top and middle) shows the overall structure and onset and progression of the 5415 sonar dome vortices, including the primary vortices SDVP, SDVS, SDVT, and SDVT2, whereas Figure 1 (bottom) shows the location for the turbulence structure and vortex breakdown and interaction analysis for the SDVP vortex core at $x/L = 0.12$. It should be recognized that the current analysis is subject to the current 4DPTV 2 – 4 mm spatial resolution, which will be addressed in future experiments via the purchase of a new lens enabling 1 mm spatial resolution. The analysis methods are largely based on Bernard (2019) and Pope (2000) with detailed derivations provided by Stern et al. (2023).

EXPERIMENTAL AND DES METHODS

Experimental Methods

Sanada et al. (2023) mainly focused on the visualization of the 3D vortical structures for 5415 sonar dome vortices and statistical comparisons with the previous TPIV (and DES) results, such that a moving average filter was used to interpolate missing data and to match the data rate with the TPIV. In this case, the filter size was determined so that the cutoff frequency of the moving average filter was 7.5 Hz, which corresponds to the Nyquist frequency of the TPIV with a sampling rate of 15 Hz. In the initial stage of this study, the temporal and spatial autocorrelation functions and energy spectrums were also evaluated using the time series data after applying the filter, but a periodic ripple attenuation due to the moving average filter can be observed in the spectrums and the overall results were under resolved compared to the unfiltered data. Therefore, the final analysis uses nearest-neighbor interpolation to interpolate the missing data in the raw data. It should be noted that almost no missing values exist (less than 0.2%) in the raw time series at the vortex core of SDVP. The time-series of one voxel is extracted mainly using the 4 mm resolution datasets, after extracting vortex cores by a 3D voxel labeling technique with sub-voxel analysis (Sanada et al., 2023). The time-series at the SDVP core at $x/L=0.12$ is used to obtain the temporal autocorrelation and energy spectrum, whereas the time series at 4.3 mm intervals upstream and downstream of $x/L=0.12$ is used to obtain the spatial autocorrelations and spectrums.

DES Methods

Bhushan et al. (2021) CFD simulations utilized the same 10M and 48M cell grids used by Bhushan et al. (2019) with a modification of the vortex core refinement grid to align it in the direction of the SDVP (previously referred to as SDTV) progression. The DES results were used to extract the time series at the SDVP core at $x/L=0.12$. The simulations of the 48M and 10M grids were performed at time-steps of $dt = 0.002L/U = 0.00398$ s. However, simulation results were written at every fourth time-step due to file size constraints. Therefore, the time-step after resampling of the DES data for the medium grid was $dt = 0.008L/U = 0.0159$ s. The temporal autocorrelation function and energy spectrum were obtained from the extracted vortex core time series using the resampled time-step size. The grid resolution near the vortex core on the YZ-plane at $x/L = 0.12$ core was approximately 4.572 mm in the y-direction and 2.438 mm in the z-direction. The Bhushan et al. (2019 and 2021) results were also contributed to the NATO AVT-253 and its predecessor AVT-183 Working Groups (NATO STO, 2017 and 2021), which used the TPIV data for validation and evaluation of the contributed prediction methods. The present DES was obtained many years ago and herein the results on the finest grids are not used. Nonetheless, in consideration of its performance compared to the other methods, the present results are representative of current state-of-the-art methods, and they are an indication of the direction needed for improvements of hybrid-RANS/LES methods.

MACRO FEATURES AND LARGE SCALES

Figure 2 shows the Q-criteria and mean axial vorticity $\langle\omega_x\rangle$ contours for the TPIV, 4DPTV, and DES. The TPIV and 4DPTV results are similar with both indicating elliptically shaped cross plane streamlines and substantial interactions between the SDVP and the other vortices, especially SDVS. The DES is similar but clearly less resolved than both experiments. Figure 2 also includes an outline of the viewing window pertaining to the 3D perspective shown later. Figure 3

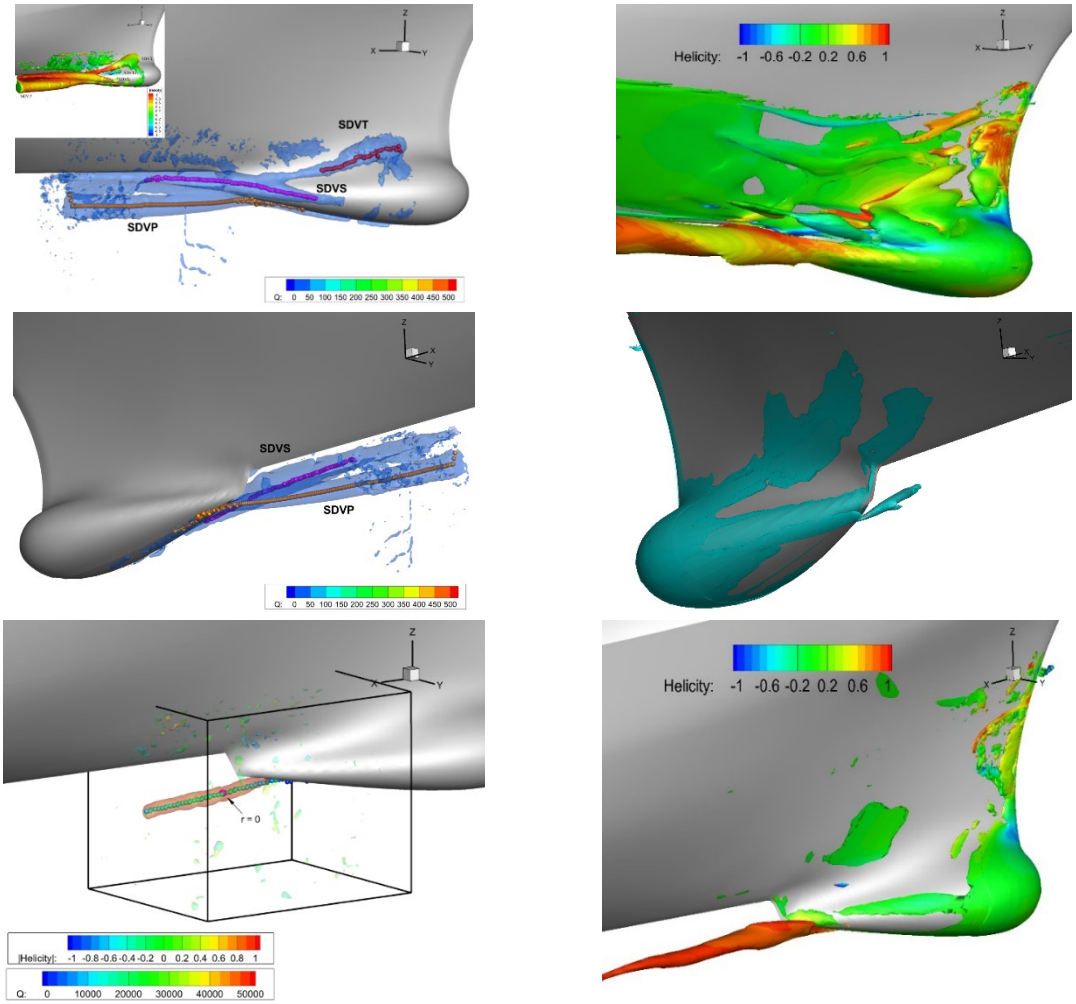

Figure 1: SDVP, SDVS, SDVT, and SDVT2 vortices (top and middle) and turbulence analysis location for SDVP core (bottom)

shows the comparisons of the normalized Q/Q_{max} and mean axial vorticity $\langle\omega_x\rangle/\langle\omega_{xmax}\rangle$ vs. *r/R* for the horizontal YY and vertical ZZ cuts through the vortex core, as indicated in Figure 2, along with Gaussian and Bell distributions for comparisons. *r* is the radial distance from the vortex core location normalized by the R=W/2 value at $Q/Q_{max} = 0.5$, where W is the half-width of the vortex. The Q/Q_{max} and $\langle\omega_x\rangle/\langle\omega_{xmax}\rangle$ distributions in Figure 3 are compared with the Gaussian function, $f(r) = e^{-(5r/3W)^2}$, and Bell function, $f(r) = (1 + |2r/w|^2)^{-1}$, respectively.

Table 1 provides the core locations and R values. Here again, the experiments show similar trends with good agreement to the distributions; however, the TPIV core location is closer to the center plane but at a similar depth, and its average R is 23% smaller than the 4DPTV. The DES shows less agreement with the distributions than the experiments, especially for the ZZ cut in the negative direction, and the core location and size are closer to the 4DPTV than the TPIV; however, its R value is nearly 40% larger than the 4DPTV and 80% larger than the TPIV. The reason for the differences in the ZZ cut is a secondary peak for the DES, which is attributed to its larger diffusion and increased interactions between the SDVP and SDVS vortices than that shown by the experiments.

Figure 4 shows the 3D contours of Q for the 4DPTV (4 mm resolution), TPIV, and the DES with overlaying meshes. The 4DPTV and TPIV indicate that the vortex patterns are nearly symmetric, whereas the DES is asymmetric, all of which are consistent with Figure 3. The 4 mm 4DPTV has less points within the vortex than the 2 mm resolution (not shown) and

the TPIV and DES. Based on these figures, the estimate of the vortex diameter, based on the Q contour level of zero, is approximately l_0 = 25 mm for the 4DPTV. In comparison, it is 14 mm for the TPIV and 30 mm for the DES. The vortex diameter estimates based on Q contour level are larger than the estimates in Table 1 (i.e., 4-5R ≈ l_0).

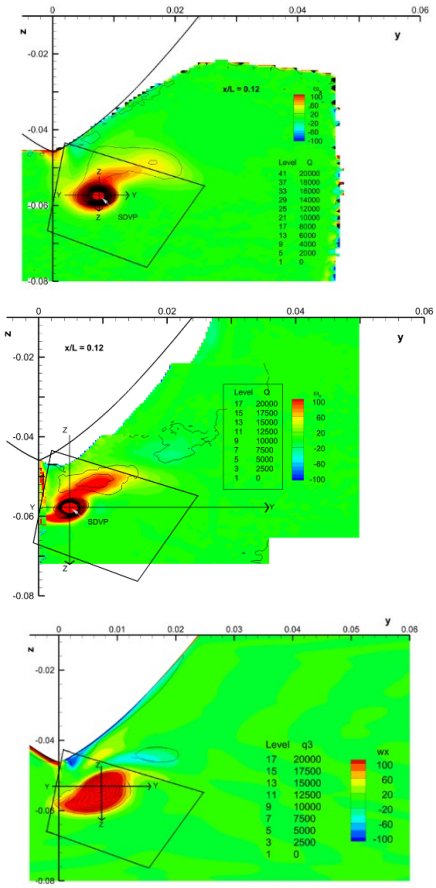

Figure 2: Axial vorticity (ω_x) contour with Q isolines for (a)4DPTV, (b)TPIV, and (c) DES.

The model scale length is L = 3.048 m, and the carriage speed is U = 1.531 m/s. The kinematic viscosity is ν = 1.182E-06 m^2/s. The Reynolds (Re) = and Froude (Fr) numbers are 3.948E06 and 0.28, respectively.

Table 2 provides the macro-scale vortex core parameters. The 4DPTV shows mean velocity <U> is 0.80U. The turbulent velocity scale u_o=k$^{1/2}$ is 17.4% of the mean velocity <U> and is on the order of the rms turbulence intensity, defined as $u' \equiv (2/3k)^{1/2}$. The turbulent length scale is defined as L = l_0/0.43 [1], resulting in Re_L = k$^{1/2}$L/ν= 10780 and a dissipation $\varepsilon = u_0^3/l_0$ = 0.181 m^2/s^3. The TPIV has 13.9% smaller <U>, 33.3% smaller <u^2> and 37.5% smaller k such that u_0 is 21% smaller. Since l_0 is 44% smaller, ε is 11.6% smaller, and the resulting Re_L is 55.7% smaller than that for the 4DPTV. The turbulence is much stronger for the 4DPTV vs. the TPIV, and both are much stronger than the DES. However, the anisotropy, which is discussed in detail later, has

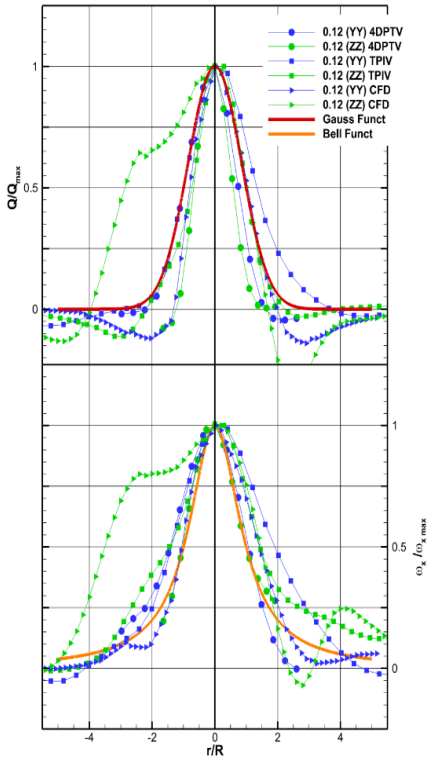

Figure 3 : Q/Q_{max} and ω_x/ $\omega_{x,max}$ Distribution Plots.

[1] By dimensional reasoning, $\varepsilon \sim u_0^3/l_0$, where l_o is the length scale representative of the largest eddies in the flow based on geometric characteristics and u_0 is their characteristic velocity, which is assumed = $\sqrt{k}$. l_0 is proportional to the Taylor macro-scale L_{11}, both representing the dimension of the vortices in the energy-containing range. To determine the relationship between the Taylor and Kolmogorov scales the turbulent length scale is defined as L = $\varepsilon/k^{3/2}$ with turbulent Reynolds number $Re_L = \frac{\sqrt{k}L}{\nu}$. The relation between L and L_{11} is obtained using the model spectrum, as per Pope (2000) Figure 6.24, showing that the ratio $\frac{L_{11}}{L} \sim 0.43$ for $Re_L = \frac{3}{20}R_\lambda^2 > 100$. We have assumed that $l_o = L_{11}$ in our analysis and therefore L = $\frac{L_{11}}{0.43} = \frac{l_0}{0.43}$. However, in retrospect, and based on our micro scale analysis l_0 shows larger values than L_{11} and it is closer to L, i.e., $L_{11}/l_0 \sim 0.35$. This result is in line with the idea that l_0 characterizes the dimension of the 3D eddies, whereas L_{11} is based on the 1D autocorrelation. For the evaluation of L, it would be more accurate to consider L = l_0, instead of using L = $l_0/0.43 = 2.33l_0$.

Table 1: Core location and vortex width on cutline distribution

Measurement	Core		$R = W/2$ at $Q/Q\_max = 0.5$			
	y [-]	z [-]	YY [-]	ZZ [-]	Mean [-]	Mean [m]
4DPTV (2mm)	0.0076	-0.0573	0.0014	0.0015	0.0015	0.0045
TPIV	0.0048	-0.0577	0.0011	0.0011	0.0011	0.0034
DES	0.00710	-0.05270	0.00200	0.00200	0.00200	0.00610

similarities of $3\langle u^2\rangle/2k = 0.56$ for the 4DPTV vs. 0.6 for the TPIV and 0.29 for the DES; and differences, i.e. $\langle v^2\rangle \approx 1.3\langle w^2\rangle \approx 2.5\,\langle u^2\rangle$ for the 4DTPV vs. $\langle v^2\rangle \approx 0.5\langle w^2\rangle \approx 1.5\,\langle u^2\rangle$ for the TPIV and $\langle v^2\rangle \approx 0.56\langle w^2\rangle \approx 3.4\,\langle u^2\rangle$ for the DES.

Table 3 provides the time mean circulation $\langle\Gamma\rangle$, normalized time mean circulation $\langle\Gamma\rangle/\langle U\rangle l_0$, time mean tangential velocity of the vortex core $\langle U_\theta\rangle$, and corresponding swirl number $S = \langle U_\theta\rangle/\langle U\rangle$. Based on Stoke's theorem, $\langle\Gamma\rangle$ is obtained by line integrating $\langle U_\theta\rangle$ along a route surrounding the vortex core, or area integration of the inner product of the time mean vorticity vector $\langle\boldsymbol{\Omega}\rangle = \big(\langle\Omega_x\rangle, \langle\Omega_y\rangle, \langle\Omega_z\rangle\big)$ and the normal vector in the *y*-*z* plane $\boldsymbol{n} = (1,0,0)$ inside the core, i.e., the summation of $\langle\Omega_x\rangle$ inside the core: $\langle\Gamma\rangle = \oint_C \langle\boldsymbol{U}\rangle \cdot d\boldsymbol{r} = \int_A \langle\boldsymbol{\Omega}\rangle \cdot \boldsymbol{n} dA = \int_A \langle\Omega_x\rangle dA$. $\langle U_\theta\rangle$ is obtained by dividing $\langle\Gamma\rangle$ by the perimeter of the line integral ($L_{perimeter}$): $\langle U_\theta\rangle = \langle\Gamma\rangle/L_{perimeter}$. Table 3 uses the average values of the two approaches.

The 4DPTV dimensional $\langle\Gamma\rangle$ is larger than the TPIV, whereas the non-dimensional $\langle\Gamma\rangle/(\langle U\rangle\, l_0)$ is smaller. The swirl numbers are all smaller for the 4DPTV than for the TPIV. Thus, the vortex strength is larger for the TPIV than for the 4DPTV. The DES shows better agreement with the 4DPTV than the TPIV, but here again with large errors. The swirl numbers are all much less than the critical values provided in the literature for vortex breakdown for wing tip ($\mathrm{Sc} \approx 2-3$) and delta wing ($\mathrm{Sc} \approx 1$) vortices. Nonetheless, as shown in Sanada et al. (2023), SDVP undergoes vortex breakdown, which, as discussed later, and is attributed to vortex-vortex interactions.

The macro-scale turbulence is larger for the 4DPTV than the TPIV, and vice-versa for the vortex strength. It is not possible to say with confidence which measurement is more accurate, as the TPIV has somewhat higher spatial resolution, whereas the 4DPTV has much higher temporal resolution and lower uncertainties. The DES shows similar trends as the experiments, but there are large quantitative differences.

SPECTRAL ANALYSIS AND SMALL SCALES

The 1D axial velocity ($u(t)$) spectral analysis and evaluation of the small scales is done using both temporal and spatial (along the time mean vortex core) autocorrelations and energy spectrums. 3D energy spectrums are also obtained from the 1D energy spectrums using isotropic tensor theory. The results are compared with model energy spectrums constructed based on both the 4DPTV and TPIV macro-scale results.

Preliminary to the analysis of the axial velocity energy spectrum, an analysis is made of its time series along the SDVP vortex core upstream and downstream of x/*L* = 0.12 and its FFT at x/*L* = 0.12, as shown in Figures 5(a)-(d). A dominant frequency is clearly observed at frequencies 10.0 and 7.47 Hz (Strouhal numbers (St=*fL/U*) are 19.9 and 14.9, respectively) for the 4DPTV and DES, respectively. The Sanada et al. (2023) analysis indicates that SDVP has helical streamlines (refer to Figures 5 and 18 in the paper for the 4DPTV and DES, respectively). The SDVP core undergoes spiral vortex breakdown followed by helical mode instability and with scaling like the previous TPIV and DES results for 5415 at β=20 deg, DES for KVLCC2 at β=30 deg, and delta wing vortices (refer to Figure 25(b) in Sanada et al. 2023). Note that the Figure 5(a)-(b) results differ from Sanada et al. (2023) Figures 24 and 25(a) since the present results do not use the moving average filter.

Table 2: Macro-scale vortex core parameters

Parameter	4DPTV	TPIV	DES
<U> [m/s]	1.255	1.081	1.313
$\langle u^2\rangle$ [m^2/s^2]	0.018	0.012	0.002
k [m^2/s^2]	0.048	0.030	0.014
u_o [m/s]	0.219	0.173	0.095
u' [m/s]	0.179	0.141	0.077
l_0 [m]	0.025	0.014	0.030
L [m]	0.058	0.033	0.070
ε [m^2/s^3]	0.181	0.160	0.012
Re_L	10780.2	4771.7	5600.5

Figure 5(c) shows the $u(x,t)$ contours upstream and downstream of x/*L* = 0.12 for -0.03 ≤ x/*L* ≤ 0.03 and 0 ≤ t ≤ 8 s; and Figure 5(d,e) shows zoomed in views for -0.03 ≤ x/*L* ≤ 0.03 and 0 ≤ t ≤ 0.5 s. The

temporal oscillations for the 4DPTV and DES are shown to occur at periods of approximately 0.1 and 0.13 s, respectively, which correspond to frequencies 10 and 7.47 Hz and are attributed to the spiral vortex breakdown/helical mode instability. Figure 5(d,e) also clearly shows the existence of $u(x,t)$ spatial waves traveling in the positive x direction. The wave speed dx/dt is estimated for the 4DPTV and DES to be 1.25 and 1.33 m/s, which coincides with their estimated mean vortex core velocities <U> shown in Table 3. The turbulence is transported by the mean velocity, which supports the later use of the Taylor hypothesis. The spatial waves are also due to the spiral vortex breakdown/helical mode instability with wavelengths λ estimated at x/L = 0.12 based on the wave speed times the wave period, i.e., λ =0.125 and 0.133 m for the 4DPTV and DES, respectively.

Temporal Spectrum

The temporal autocorrelation function:

$$R_E(\tau) = \frac{\langle u(t)u(t+\tau)\rangle}{\langle u^2\rangle}, \quad (1)$$

is shown in Figure 6(a) and its Fourier transform $\hat{R}_E(2\pi\omega)$ is given by Equation (2).

$$\hat{R}_E(2\pi\omega) = 2\int_0^\infty R_E(\tau)\cos(2\pi\omega\tau)\,d\tau$$

$$= \frac{1}{u^2}\lim_{T\to\infty}\frac{1}{2T}\underbrace{\int_{-T}^{T} u(t)e^{-i\omega' t}dt}_{\boxed{\hat{u}(\omega)}}\underbrace{\int_{-\infty}^{\infty} u(t)e^{i\omega' t}dt}_{\boxed{\hat{u}^*(\omega)}}, \quad (2)$$

$\hat{R}_E(2\pi\omega)$ is shown in Figure 7(a) (note that ω is the frequency in Hz and $\omega' = 2\pi\omega$ in rad/s). The second equality in Equation (2) shows that $\hat{R}_E(\omega')$ can also be computed using the Fourier transform pair for $u(t)$ and its complex conjugate where the limit is taken using the duration of the 4DPTV and DES time series for $u(t)$.

The temporal micro and macro (τ_E and T, respectively) scales are given by Equations (3) and (4).

$$\tau_E = \left[\frac{-2}{f''(0)}\right]^{\frac{1}{2}}, \quad (3)$$

$$T = \int_0^\infty R_E(\tau)\,d\tau \quad (4)$$

The Taylor micro, λ_f, and macro, Λ_f, length scales are calculated using the Taylor hypothesis and the resulting dissipation ε and Kolmogorov length scale η are:

$$\lambda_f = \bar{U}\tau_E, \quad (5)$$

$$\Lambda_f = \bar{U}T, \quad (6)$$

$$\varepsilon = \frac{30\nu u'^2}{\lambda_f{}^2}, \quad (7)$$

$$\eta = \left(\frac{\nu^3}{\varepsilon}\right)^{\frac{1}{4}}, \quad (8)$$

Table 4 provides the values for the micro-scale vortex core parameters τ_E, T, λ_f, Λ_f, $R_\lambda = u'\lambda_g/\nu$ (where $\lambda_g = \lambda_f/\sqrt{2}$), ε, and η.

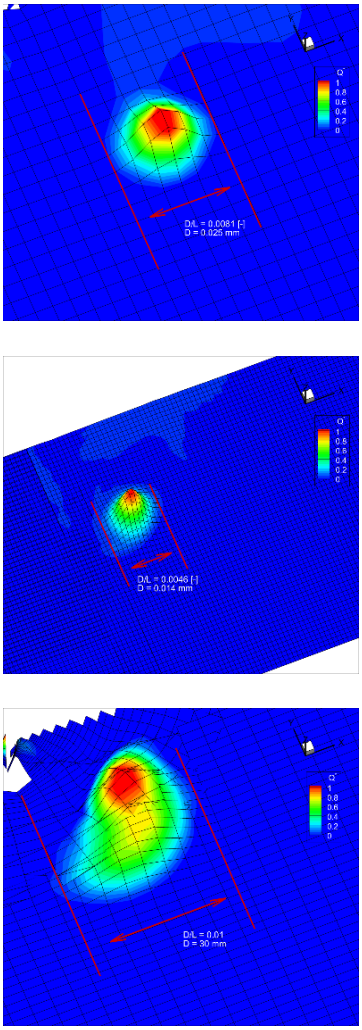

(a)

(b)

(c)

Figure 4: Q/Q_{max} 3D Contour with Mesh for (a) 4DPTV 4mm, (b) TPIV, and (c) DES

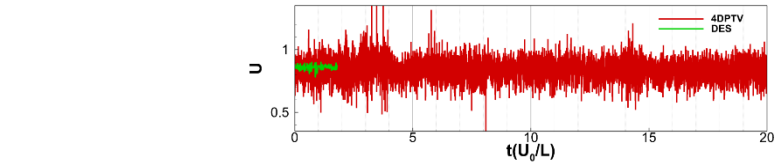

(a)

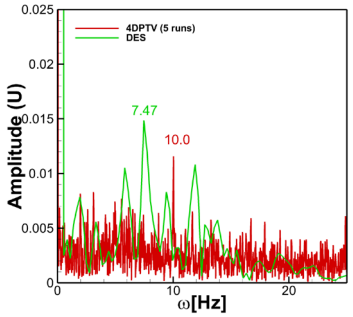

(b)

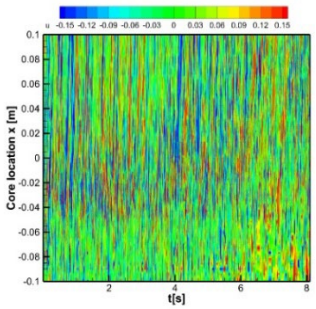

(c) 4DPTV

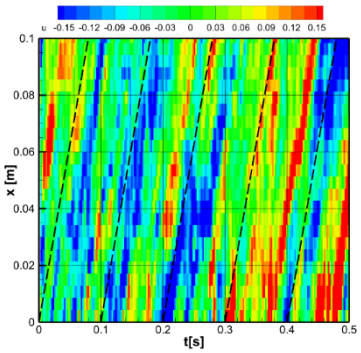

(d) 4DPTV (Dotted lines: dx/dt = 1.25)

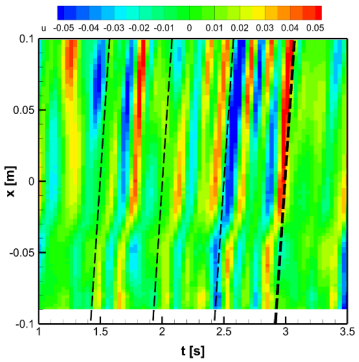

(e) DES (Dotted lines: dx/dt = 1.33)

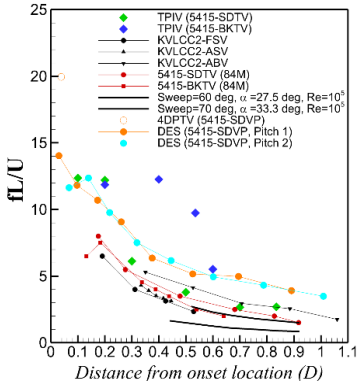

(f)

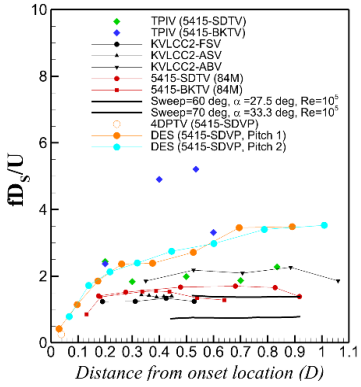

(g)

Figure 5: $u(t)$ at SDVP core: time series (a) and FFT analysis (b) at x/L = 0.12 (b); $u(x,t)$ vs. time and space upstream and downstream of x/L = 0.12 (c,d,e); and variation of St and St_{DS} (=fD_S/U) vs. distance from onset (f,g).

Figures 7(b) and (c) show the 1D energy spectrum in time $\hat{E}_{11}(\omega)$ and space $E_{11}(k_1)$, respectively, in the latter case using the Taylor hypothesis:

$$\hat{E}_{11}(\omega) = 2\langle u^2\rangle \hat{R}_E(2\pi\omega) = \lim_{T\to\infty}\frac{1}{T}|\hat{u}(\omega)|^2, \quad (9)$$

$$E_{11}(k_1) = \frac{\bar{U}}{2\pi}\hat{E}_{11}(\omega), \quad (10)$$

where $k_1 = 2\pi\omega/\bar{U}$. The second equality in Equation (9) shows that $\hat{E}_{11}(\omega)$ can also be computed from $|\hat{u}(\omega)|^2$, i.e., power spectral density or convolution integral approach in contrast to using the temporal autocorrelation.

Table 3: Vortex circulation and swirl numbers

Parameter	4DPTV	TPIV	DES
$\langle\Gamma\rangle$ [m^2/s]	0.0302	0.0226	0.0341
$\langle\Gamma\rangle/(\langle U\rangle l_0)$ [-]	0.9683	1.4650	0.8808
$\langle U_\theta\rangle$ [m/s]	0.3533	0.3748	0.2229
$\langle U_\theta\rangle/U$ [-]	0.2308	0.2448	0.1456
$S=\langle U_\theta\rangle/\langle U\rangle$ [-]	0.2829	0.3398	0.1740

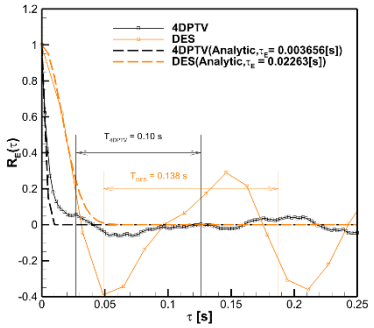

(a)

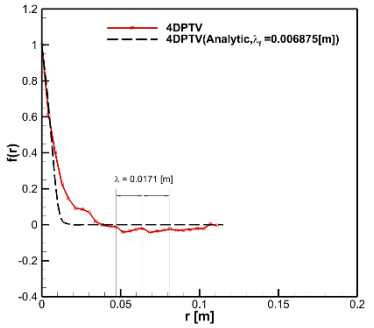

(b)

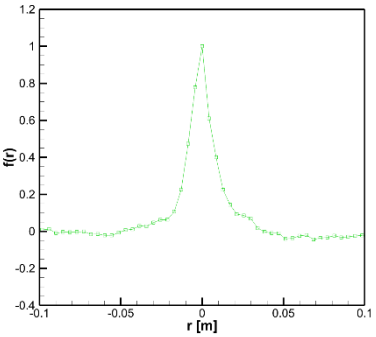

(c)

Figure 6: Longitudinal autocorrelation: (a) temporal with analytic function $R_E(\tau)=e^{-\tau^2/{\tau_E}^2}$, (b) symmetric with $f(r)=e^{-r^2/{\lambda_f}^2}$, and (c) unsymmetric.

Figure 8(a) shows the Kolmogorov $\left(E_{11}(k_1)/(\varepsilon\nu^5)^{1/4}\right)$ and Figures 8(b) and (c) shows the compensated $\left(\varepsilon^{-2/3}k_1^{5/3}E_{11}(k_1)\right)$ spectrums vs. $k_1\eta$ using log/linear and linear/log scaling, respectively.

Spatial Spectrum: Symmetric $f(r)$ and Isotropic ε

The symmetric/homogeneous spatial autocorrelation function, $f(r)$, is given by

$$f(r)=\frac{\langle u(x)u(x+r)\rangle}{\langle u^2\rangle}, \tag{11}$$

and is shown in Figure 6(b). Its Fourier transform, $E_{11}(k_1)$, is calculated by

$$E_{11}(k_1)=\frac{2}{\pi}\langle u^2\rangle\int_0^\infty f(r_1)\,cos(k_1r_1)\,dr_1, \tag{12}$$

and is plotted in Figure 7(c). The Taylor micro and macro length scales are given by Equations (13) and (14).

$$\lambda_f=\left[\frac{-2}{f''(0)}\right]^{\frac{1}{2}}, \tag{13}$$

$$\Lambda_f=\frac{1}{2}\int_{-\infty}^{\infty}f(r)\,dr=\int_0^\infty f(r)\,dr, \tag{14}$$

Table 4 provides the values for the micro-scale vortex core parameters and Figure 8 shows the Kolmogorov and compensated spectrums.

Spatial Spectrum: Asymmetric $f(\pm r)$ and Anisotropic ε

The asymmetric/non-homogeneous spatial autocorrelation function, $f(\pm r)$, is given by

$$f(r)=\frac{\langle u(x)u(x\pm r)\rangle}{\langle u^2\rangle}, \tag{15}$$

and is shown in Figure 6(c). Its Fourier transform, $E_{11}(k_1)$, is calculated by

$$E_{11}(k_1)=\frac{\langle u^2\rangle}{\pi}\int_{-\infty}^{\infty}f(r_1)\,cos(k_1r_1)\,dr_1, \tag{16}$$

and is plotted in Figure 7(c). The Taylor micro and macro length scales are given by Equations (17) and (18), respectively.

$$\lambda_f = \frac{\left[-f'(0) - \left[\left\{f'(0)\right\}^2 - 2f''(0)\right]^{\frac{1}{2}}\right]}{f''(0)}, \quad (17)$$

$$\Lambda_f = \frac{1}{2}\int_{-\infty}^{\infty} f(r)\, dr, \quad (18)$$

Equation (17) is equivalent to Equation (13) if $f'(0)$ is equal to zero, which is true if the autocorrelation function is symmetric. The dissipation is calculated directly from its definition in Equation (19) with the repeated index implying summation.

$$\varepsilon = \nu\left(\frac{\partial u_i}{\partial x_j}\frac{\partial u_i}{\partial x_j} + \frac{\partial u_i}{\partial x_j}\frac{\partial u_j}{\partial x_i}\right), \quad (19)$$

Figure 9 summarizes the results of the direct calculation of ε, and η is calculated from Equation (8). Table 4 provides the values for the micro-scale vortex core parameters and Figure 8 shows the Kolmogorov and compensated spectrums.

Model and 3D Spectrum

The 3D model spectrum is defined as:

$$E(\kappa) = C\varepsilon^{\frac{2}{3}}\kappa^{-\frac{5}{3}} f_L(\kappa L) f_\eta(\kappa\eta), \quad (20)$$

$$f_L(\kappa L) = \left(\frac{\kappa L}{[(\kappa L)^2 + c_L]^{\frac{1}{2}}}\right)^{\frac{5}{3}+p_0}, \quad (21)$$

$$f_\eta(\kappa\eta) = exp\left\{-\beta\left\{\left[(\kappa\eta)^4 + {c_\eta}^4\right]^{\frac{1}{4}} - c_\eta\right\}\right\}, \quad (22)$$

with the Table 2 values used for L and k. A model spectrum was evaluated for both the 4DPTV and TPIV values. The values of the coefficients $C = 1.5$, $p_0 = 2$, $\beta = 5.2$, $c_L \approx 6.78$, and $c_\eta \approx 0.40$ are the suggested values for high Re. However, c_L and c_η can be determined by ensuring that the integrals of $E(\kappa)$ and $2\nu\kappa^2 E(\kappa)$ over the entire wavenumber range recover k and ε, respectively. This process was done by a trial-and-error method which varied the c_L and c_η values and evaluated the integrals numerically. Values of $c_L = 5.76$ and $c_\eta = 0.40\, c_L$ were determined to be best for both 4DPTV and TPIV. Benchmark (BM) comparison values based on the model spectrum and scaling estimates for λ_f, Λ_f, R_λ, ε, and η are as follows:

$$\lambda_f = \sqrt{20} L {Re_L}^{-\frac{1}{2}}, \quad (23)$$

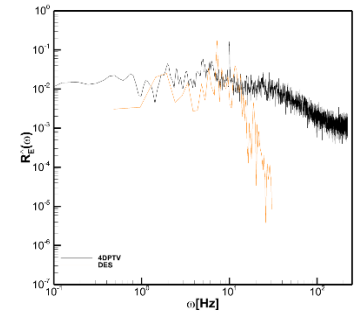

(a)

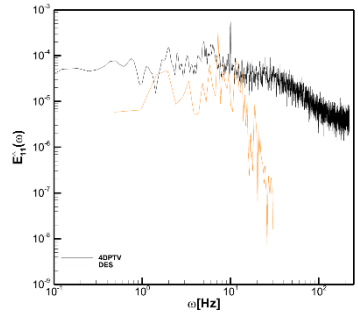

(b)

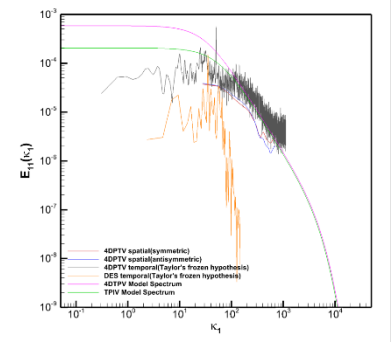

(c)

Figure 7: (a) Temporal autocorrelation: Fourier transform, (b) temporal 1D energy spectrum, and (c) spatial 1D energy spectrum.

$$\Lambda_f = L_{11}, \quad (24)$$

$$R_\lambda = \frac{k^{\frac{1}{2}}\lambda_f}{\sqrt{2}\nu}, \quad (25)$$

$$\varepsilon = \frac{30\nu {u'}^2}{{\lambda_f}^2}, \quad (26)$$

$$\eta = \left(\frac{\nu^3}{\varepsilon}\right)^{\frac{1}{4}}, \quad (27)$$

Table 4: 4DPTV micro-scale vortex core parameters

Parameter	4DPTV BM	Temporal 4DPTV	Spatial Symmetric	Spatial Asymmetric and Anisotropic	TPIV BM	DES Temporal
λ_f [m]	2.50E-03	4.59E-03	6.87E-03	7.20E-03	2.11E-03	3.48E-02
Λ_f[m] =L_{11}=l_o	2.50E-02	7.59E-03	8.69E-03	9.63E-03	1.40E-02	4.60E-02
R_λ	3.27E+02	4.92E+02	7.35E+02	7.71E+02	2.19E+02	1.61E+03
ε [m^2/s^3]	1.81E-01	5.38E-02	2.40E-02	2.19E-02	1.60E-01	1.76E-04
η [m]	5.50E-05	7.44E-05	9.10E-05	9.32E-05	5.70E-05	3.11E-04

These values are included in Table 4 for the 4DPTV and TPIV. Additional estimates for L_{11} values for 4DPTV and TPIV are obtained from the model spectrum using the integral relationship for isotropic turbulence shown in Equation (28).

$$L_{11} = \frac{3\pi}{4k}\int_0^\infty \frac{E(\kappa)}{\kappa}\,d\kappa, \qquad (28)$$

Both values were approximately 15% larger than the macro-scale estimate counterparts.

The 1D model energy spectrum can be obtained from the 3D model spectrum under isotropic turbulence assumptions as follows:

$$E_{11}(\kappa_1) = \int_{\kappa_1}^\infty \frac{E(\kappa)}{\kappa}\left(1 - \frac{{\kappa_1}^2}{\kappa^2}\right)d\kappa. \qquad (29)$$

The integration was done numerically within a loop over increasing values of κ_1 to obtain the 1D model spectrum as a function of κ_1 values. This is done to account for contributions from all wavenumbers κ greater than κ_1 to $E_{11}(\kappa_1)$, a phenomenon referred to as aliasing. Equations (29) or (10), (12), and (16) can be inverted using isotropic turbulence theory to determine the three-dimensional energy spectrum from the $E_{11}(\kappa_1)$ spectrums as given by Equation (30)

$$E(\kappa) = \frac{1}{2}\kappa^3\frac{d}{d\kappa}\left(\frac{1}{\kappa}\frac{dE_{11}(\kappa)}{d\kappa}\right), \qquad (30)$$

which was used and similarly evaluated to convert the experimental $E_{11}(\kappa_1)$ to its corresponding 3D spectrum $E(\kappa)$.

Discussion

The DES employed only the power spectral density/convolution integral approach for temporal analysis, while 4DPTV utilized both the temporal autocorrelation and power spectral density/convolution integral approaches, both of which yielded identical results.

The 4DPTV data rate is 444.2 Hz such that the temporal resolution is equal to 0.00225 s. The data acquisition time interval is about 8 s such that the number of images per towing tank carriage run is about 8 × 444.2 ≈ 3600. Therefore, the 4DPTV resolution limitations are ω_{min} = 444.2/3600 = 0.123 Hz and ω_{max} = 444.2/2 = 222 Hz. Converting these values to wavenumber space, $\kappa_{1min} = 2\pi\omega_{min}/\langle U\rangle$ = 0.618 m^{-1} and $\kappa_{1max} = 2\pi\omega_{max}/\langle U\rangle$ = 1111.95 m^{-1}, and the length scale values are $l_{1min} = 2\pi/\kappa_{1max}$ = 0.006 m and $l_{1max} = 2\pi/\kappa_{1min}$ = 10.171 m. The data acquisition time interval of the DES is approximately 3.60 s Therefore, the DES has frequency limitations of ω_{min} = 1/3.60 = 0.278 Hz and ω_{max} = 1/ (2×0.0159) = 31.1 Hz. In wavenumber space these values are $\kappa_{1min} = 2\pi\omega_{min}/\langle U\rangle$ = 1.329 m^{-1} and $\kappa_{1max} = 2\pi\omega_{max}/\langle U\rangle$ = 148.92 m^{-1}, and the corresponding length scales are $l_{1min} = 2\pi/\kappa_{1max}$ = 0.042 m and $l_{1max} = 2\pi/\kappa_{1min}$ = 4.729 m. The intervals between the points for the 4DPTV and DES in Figure 6(a) correspond to the previously mentioned dt intervals, and the t_{max} of the 4DPTV is truncated to match the DES t_{max} according to the DES data acquisition interval. The 4DPTV and DES Figures 7(a) and (b) ω_{min} and ω_{max} and Figure 7(c) κ_{1min} and κ_{1max} values similarly correspond the values detailed above.

The 4DPTV spatial resolution used for the current analysis is about 0.004277 m such that l_{1min} = 2dx = 0.009 m and l_{1max} = 0.222 m, the latter of which corresponds to the length of the measurement volume The corresponding κ_{1min} and κ_{1max} values are 28.303 m^{-1} and 734.532 m^{-1}, respectively. The 4DPTV Figure 6(b) and (c) dr intervals and r_{max} correspond to the previously mentioned dx and l_{1max} values, respectively; however, the r_{max} value of Figures 6(b) and (c) are truncated at 0.2 m and 0.1 m, respectively. The 4DPTV Figure 7(c) spatial spectrum κ_{1min} and κ_{1max} values correspond to previously mentioned values. As already mentioned, the DES spatial resolution is 4.572 mm.

Both the 4DPTV and DES temporal autocorrelations, as shown in Figure 6(a), exhibit the anticipated Gaussian profile for small values of τ. Additionally, they display oscillations for τ greater than approximately 0.02 s and 0.03 s, respectively.

These observations align closely with the analytical solution of the dissipation range, $\exp(-t^2/\tau_E^2)$, for τ values preceding the onset of the oscillations. The periods of the 4DPTV and DES oscillations are 0.1 s and 0.138 s, respectively, which correspond to their peaks in Figure 5(b), as discussed earlier, and Figures 7(a)-(c) and Figure 8(a), to be discussed.

The 4DPTV and DES Figure 7(a) $\hat{R}_E(2\pi\omega)$ and Figure 7(b) $\hat{E}_{11}(\omega)$ show similar trends for $\omega < 15$ Hz, although the DES magnitudes are somewhat and significantly smaller for $\hat{R}_E(2\pi\omega)$ and $\hat{E}_{11}(\omega)$, respectively, and in both cases clearly less resolved. The larger differences for $\hat{E}_{11}(\omega)$ than $\hat{R}_E(2\pi\omega)$ are due to the differences in their scaling and the much larger $\langle u^2 \rangle$ for the 4DPTV vs. the DES. The 4DPTV and DES show clear peaks around 10 and 7.47 Hz, respectively, as per Figure 5(b) and the oscillations in Figure 6(a). For $\omega > 15$ Hz, the 4DPTV shows gradual dissipation, whereas the DES shows rapid dissipation and much less resolution. The frequency resolution of DES is degraded compared to 4DPTV because of the duration of DES time series data being shorter than that of the 4DPTV (initially stored in HPC but discarded due to resource limitation). The resampling of the DES with a larger time-step also degrades the frequency resolution. A longer duration and/or a finer time step of the DES data set is required to improve the frequency resolution. A finer grid would also improve the resolution.

Figure 6(b) $f(r)$ shows a Gaussian shape and good agreement with the dissipation range analytical solution $\exp(-r^2/\lambda_f^2)$. Figure 6(c) $f(\pm r)$ shows an asymmetric Gaussian shape, which needs analysis as to the nature of its asymmetry. Both distributions show periodic behavior with wavelength λ = 0.0171 m, which is attributed to the previously discussed vortex breakdown, as discussed later.

Figure 7(c) $E_{11}(\kappa_1)$ shows all four spectrums (4DPTV and DES temporal and 4DPTV symmetric/isotropic and asymmetric/anisotropic); and includes both the 4DPTV and TPIV model spectrums. The trends for the temporal spectrums using the Taylor hypothesis are similar as discussed for $\hat{R}_E(2\pi\omega)$ and $\hat{E}_{11}(\omega)$; however, $E_{11}(\kappa_1)$ shows that the 4DPTV resolves a larger portion of the inertial subrange with the Kolmogorov -5/3 slope, whereas the DES is only able to partially resolve the inertial sub range and then dissipates rapidly. The rapid dissipation is likely because of the lack of filter/grid resolution as often exhibited in LES. The spatial spectrum ranges are limited to the inertial sub-range, showing less energy than the 4DPTV temporal spectrum using the Taylor hypothesis, and exhibit kinks in the region of their largest wave numbers, which is attributed to the 4DPTV minimum spatial resolution. The 4DPTV and TPIV model spectrums overlap in the inertial and dissipation ranges, whereas the 4DPTV has larger magnitudes than the TPIV in the energy containing ranges as expected due to its larger u' value. The 4DPTV temporal spectrum using the Taylor hypothesis shows better agreement with the TPIV model spectrum than the 4DPTV model spectrum.

The benchmark λ_f is 2.5 mm which is about half the size of the 4DPTV spatial resolution used for the present analysis. Therefore, the current 4DPTV spatial resolution is insufficient as sub-millimeter spatial resolution is required to resolve the Taylor micro-scale. This is seen in the spatial symmetric and asymmetric results for λ_f, which were approximately twice the spatial resolution and almost three times larger than the benchmark. The 4DPTV temporal resolution is also too large as the smallest resolvable length scale mentioned earlier was 0.006 m which explains why the temporal micro-scale from the autocorrelation function is almost twice as large as the benchmark.

The spatial and temporal L_{11} values reported in Table 4 are smaller than the Table 2 l_0 values. This is attributed to l_0 representing the size of the largest eddies of the flow whereas L_{11} is a measure of the largest eddies along the vortex core. This is an important distinction, as the turbulent fluctuations of u are weaker than v and w along the vortex core. In contrast, l_0 and L_{11} are roughly equivalent for isotropic turbulence as the eddy size is not directionally dependent.

The R_λ, ε, and η values in Table 4 differ solely due to the discrepancies of the Taylor micro-scale since the macro-scale values are the same between each analysis and the benchmark. The R_λ values have identical difference compared with the benchmark as the λ_f results since R_λ scales directly with λ_f. The ε values for the temporal and spatial micro-scales are smaller than the benchmark value due to ε being inversely proportional to λ_f^2. Therefore, the larger λ_f values for the temporal and spatial analyses

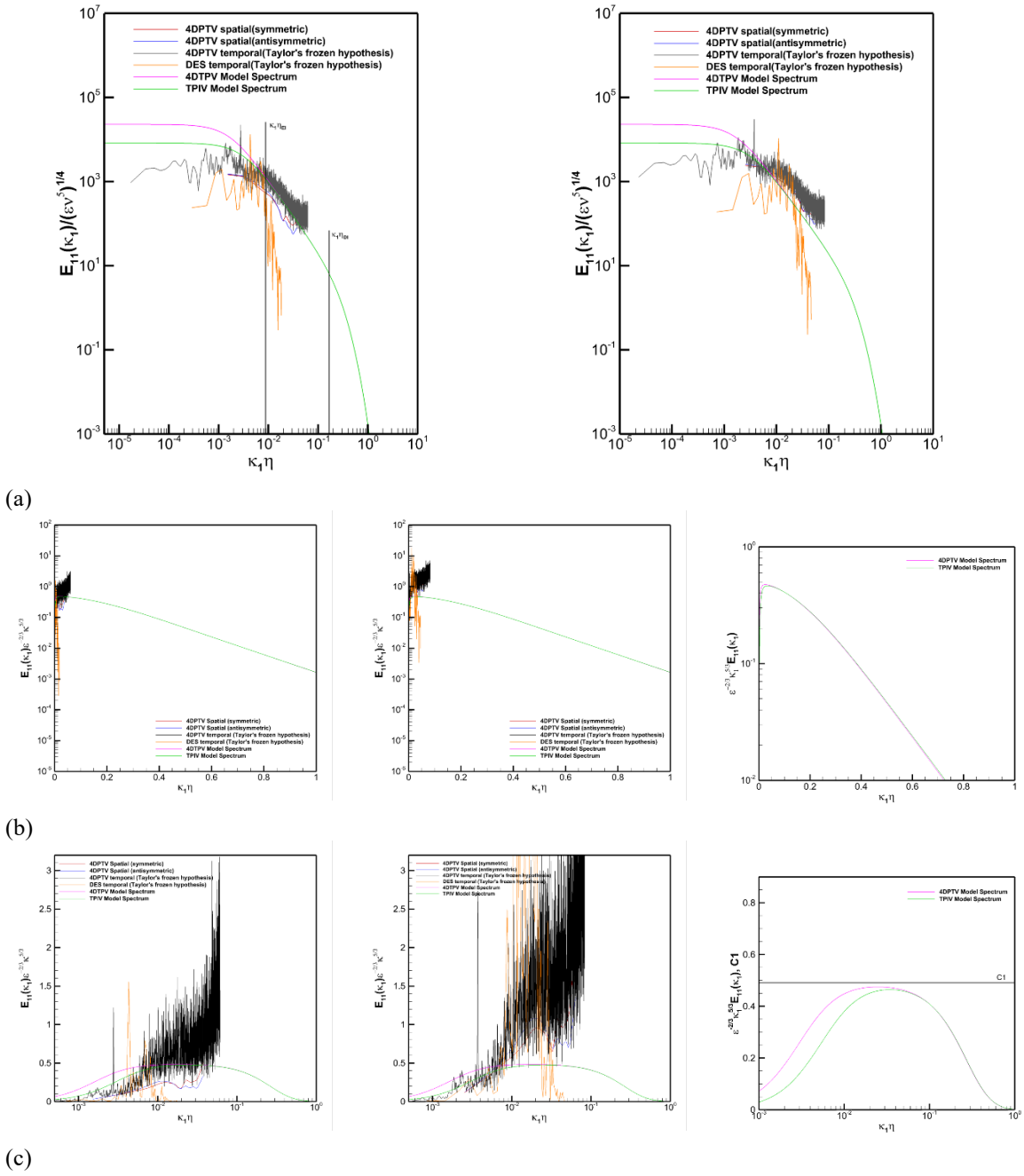

Figure 8: 1D longitudinal velocity spectra shown for (a) Kolmogorov scaling using (left) macro-scale values and (right) micro-scale values, (b) log/linear compensated scaling using (left) macro-scale values, (middle) micro-scale values, and (right) model spectra only, and (c) linear/log compensated scaling using (left) macro-scale values, (middle) micro-scale values, and (right) model spectra only.

resulted in an underprediction of the ε. Both the temporal and spatial results for η had much smaller differences relative to the benchmark values. This is attributed to the η being proportional to $\lambda_f^{1/2}$ instead of λ_f.

Table 4 provides micro-scale benchmarks based on the macro-scales of the 4DPTV and TPIV measurements and micro-scale results for the 4DPTV and DES. Both the micro-scale benchmark estimates for the 4DPTV and TPIV are of similar orders of magnitude; however, the TPIV estimates for the Taylor micro and macro-scales and turbulent Reynolds number are smaller and its Kolmogorov

length scale is larger. As observed for the 4DPTV the λ_f benchmark is based on the order of their spatial resolutions. This reiterates the need for a sub-millimeter spatial resolution to resolve the Taylor micro-scale. The η estimates are 0.550 and 0.567 mm for the 4DPTV and TPIV, respectively (note that the diameter of human hair is about 17-181 μm).

Isotropic relationships for elements of the dissipation tensor components prior to contraction are:

$$\left\langle\left(\frac{\partial u}{\partial x}\right)^2\right\rangle = \left\langle\left(\frac{\partial v}{\partial y}\right)^2\right\rangle = \left\langle\left(\frac{\partial w}{\partial z}\right)^2\right\rangle, \quad (31)$$

$$\left\langle\left(\frac{\partial u}{\partial y}\right)^2\right\rangle = \left\langle\left(\frac{\partial u}{\partial z}\right)^2\right\rangle = \left\langle\left(\frac{\partial v}{\partial x}\right)^2\right\rangle = \left\langle\left(\frac{\partial w}{\partial y}\right)^2\right\rangle = \left\langle\left(\frac{\partial v}{\partial z}\right)^2\right\rangle = \left\langle\left(\frac{\partial w}{\partial x}\right)^2\right\rangle = 2\left\langle\left(\frac{\partial u}{\partial x}\right)^2\right\rangle, \quad (32)$$

$$\left\langle\frac{\partial u}{\partial y}\cdot\frac{\partial v}{\partial x}\right\rangle = \left\langle\frac{\partial u}{\partial z}\cdot\frac{\partial w}{\partial x}\right\rangle = \left\langle\frac{\partial v}{\partial z}\cdot\frac{\partial w}{\partial y}\right\rangle = -\frac{1}{2}\left\langle\left(\frac{\partial u}{\partial x}\right)^2\right\rangle, \quad (33)$$

However, as shown in Figure 9, the elements of the dissipation tensor components prior to contraction mostly show large anisotropy. $\langle(\partial w/\partial z)^2\rangle \approx \langle(\partial u/\partial x)^2\rangle$ shows isotropic behavior, whereas $\langle(\partial v/\partial y)^2\rangle \approx 2\langle(\partial u/\partial x)^2\rangle$. $\langle(\partial v/\partial x)^2\rangle \approx \langle(\partial v/\partial z)^2\rangle \approx 2\langle(\partial u/\partial x)^2\rangle$ shows isotropic behavior, whereas $\langle(\partial u/\partial y)^2\rangle \approx \langle(\partial u/\partial z)^2\rangle \approx \langle(\partial w/\partial x)^2\rangle \approx \langle(\partial w/\partial y)^2\rangle \approx \langle(\partial u/\partial x)^2\rangle$. $\langle\partial u/\partial y \cdot \partial v/\partial x\rangle$ is over an order of magnitude smaller and $\langle\partial u/\partial z \cdot \partial w/\partial x\rangle \approx \langle\partial v/\partial z \cdot \partial w/\partial y\rangle$ are half an order of magnitude smaller than the isotropic behavior, i.e., should = $-\frac{1}{2}\langle(\partial u/\partial x)^2\rangle$.

Figure 8(a) is equivalent to 7(c) but with Kolmogorov scaling and, here again, includes the 4DPTV and TPIV model spectrums for comparison. Figure 8(a) left and right use the macro and micro-scale 4DPTV values, respectively, for the dissipation and Kolmogorov length scale. Clearly using the macro-scale values provides a more reasonable presentation of the results, as is also the case for the compensated spectrum results shown in Figures 8(b) and (c). It should be noted that the model spectrums for the 4DPTV and TPIV overpredict the energy magnitude (i.e. $\langle u^2\rangle$) within the energy-containing range as isotropic turbulence assumptions scale the model spectrum by u'^2.

The κ_1 values corresponding to the beginning of the inertial subrange, $\kappa_{1,EI}$ = 160 m^{-1}, and dissipation range, $\kappa_{1,DI}$ = 1910 m^{-1}, are labeled in Figure 8(a). In isotropic turbulence, 80% of the turbulent kinetic energy is contained within the range of $1/6L_{11} < l < 6L_{11}$. To determine the demarcation of the inertial subrange in κ_1 space, a similar criteria was used, and the $k_{1,EI}$ values correspond to the range (i.e. $0 < k_1 < \kappa_{1,EI}$) containing 80% of the integral value of the model E_{11} spectrum, u'^2. The beginning of the dissipation range is estimated to be at 60η, based on Kolmogorov's hypothesis of local isotropy. From the proposed analysis, the 4DPTV can resolve a large portion of the inertial subrange including the correct Kolmogorov constant. The linear behavior observed for large wave numbers ($\kappa_1\eta > 0.3$) indicates exponential decay.

TURBULENCE ANISOTROPY

Reynolds Stress, Anisotropic Tensor, and Realizability

Schumann (1977) investigated the realizability of Reynolds-stress turbulence models and in doing so provided the following realizability conditions for the Reynolds stress tensor based on the physical considerations discussed below:

$$\mathcal{R}_{ij} \geq 0 \quad for\ i = j, \quad (34)$$

$$\mathcal{R}_{ij}^2 \leq \mathcal{R}_{ii}\mathcal{R}_{jj} \quad for\ i \neq j, \quad (35)$$

$$\det(\mathcal{R}_{ij}) \geq 0. \quad (36)$$

Equation (34) is a consequence of real velocities, and it requires nonnegative energy. Equation (35) is a consequence of the Schwarz' inequality and it states that the cross-correlation between the velocity components u_i and u_j is bounded by the magnitude of the autocorrelations. Equation (36) states that the three cross-correlations cannot take on arbitrary values. These three equations represent five checks.

However, it is also shown that if a stronger condition is satisfied, i.e., if $\mathcal{R}_{ij}$ is a positive semi-definite matrix:

$$Q = x_i\mathcal{R}_{ij}x_j \geq 0, \quad (37)$$

for arbitrary real nonvanishing vectors x_i then not only are Equations (34) - (36) satisfied but additionally nonnegative eigenvalues and principal invariants are implied. The necessary and sufficient conditions for the positive semi-definiteness of $\mathcal{R}_{ij}$ for $i, j = \{1,2,3\}$ are the following.

$$\begin{gathered}\overline{u_i u_i} \geq 0, \\ \overline{u_i u_i} + \overline{u_j u_j} \geq 2\left|\overline{u_i u_j}\right|, \\ \det(\mathcal{R}_{ij}) \geq 0\end{gathered} \tag{38}$$

Equation (38) has the advantage of only requiring three checks vs. five for Equations (34)-(36).

The Reynolds stresses can be decomposed into their isotropic and anisotropic components:

$$R_{ij} = a_{ij} + \frac{2}{3} k \delta_{ij}, \tag{39}$$

where a_{ij} is the anisotropic Reynolds stress tensor and k is the turbulent kinetic energy. a_{ij} can be normalized using a factor equal to $2k$ to obtain the normalized anisotropic Reynolds stress b_{ij}:

$$b_{ij} = \frac{a_{ij}}{2k}. \tag{40}$$

The conditions for the positive semi-definiteness of the Reynolds stress tensor can also be expressed as constraints on the values of b_{ij} (Banerjee et al., 2007):

$$-\frac{1}{3} \leq b_{11}, b_{22}, b_{33} \leq \frac{2}{3} \text{ and } -\frac{1}{2} \leq b_{ij} \leq \frac{1}{2}, i \neq j, \tag{41}$$

which was confirmed to be satisfied by the 4DPTV, TPIV, and DES.

Lumley Triangle, Anisotropic Invariant Map (AIM) and Reynolds Stress Ellipsoid

The eigenvalue problem for R_{ij} and b_{ij} provides their characteristic equations (cubic polynomials) with three principal invariants which are independent of reference frame and functions of their respective components, i.e., $\overline{u_i u_i}$ and $\frac{a_{ij}}{2k}$, respectively. The solutions to the cubic polynomials provide the eigenvalues and eigenvectors for R_{ij} and b_{ij}, which must be real because of the realizability conditions. The eigenvalues are the principal values (i.e. the magnitude of the normal stresses in the principal axes), and the eigenvectors are the principal directions for R_{ij} and b_{ij}. The R_{ij} and b_{ij} cubic polynomials and invariants as a function of their components are given by:

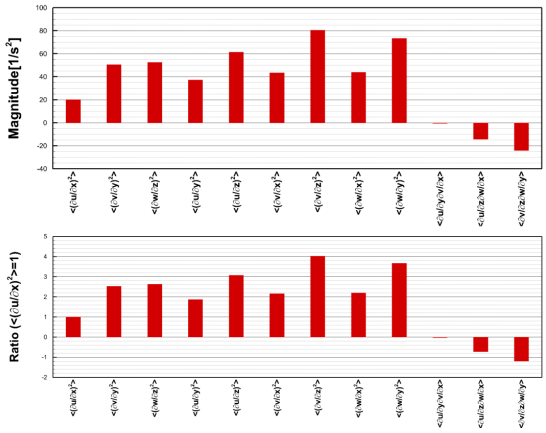

Figure 9: Dimensional and normalized by $\langle(\partial u/\partial x)^2\rangle$ dissipation components.

$$\lambda^3 - I_\delta \lambda^2 + II_\delta \lambda - III_\delta = 0, \tag{41}$$

where I_δ, II_δ, and III_δ are given by Equations (42)-(44).

$$I_\delta = \delta_{11} + \delta_{22} + \delta_{33} = \lambda_{\delta_1} + \lambda_{\delta_2} + \lambda_{\delta_3}, \tag{42}$$

$$\begin{aligned} II_\delta &= \delta_{11}\delta_{33} + \delta_{22}\delta_{33} + \delta_{11}\delta_{22} - \delta_{23}\delta_{32} - \delta_{12}\delta_{21} \\ &\quad - \delta_{13}\delta_{31} \\ &= \lambda_{\delta_1}\lambda_{\delta_3} + \lambda_{\delta_2}\lambda_{\delta_3} + \lambda_{\delta_1}\lambda_{\delta_2}, \end{aligned} \tag{43}$$

$$\begin{aligned} III_\delta &= \delta_{11}\delta_{22}\delta_{33} - \delta_{11}\delta_{23}\delta_{32} - \delta_{12}\delta_{21}\delta_{33} \\ &\quad + \delta_{12}\delta_{23}\delta_{31} \\ &\quad + \delta_{13}\delta_{21}\delta_{32} - \delta_{13}\delta_{31}\delta_{22} \\ &= \lambda_{\delta_1}\lambda_{\delta_2}\lambda_{\delta_3}, \end{aligned} \tag{44}$$

δ_{ij} can be either R_{ij} or b_{ij}. The system of equations presented in Equations (42) - (44) shows the non-linear relation between the nine components of a 2nd order tensor and its corresponding eigenvalues.

Since b_{ij} has zero trace, only two of its invariants/eigenvalues are independent. Additionally, the eigenvalues of R_{ij}, here referred to as λ_{u_i}, are related to the eigenvalues of b_{ij} as follows:

$$\lambda_{b_i} = -\frac{1}{3} + \frac{\lambda_{u_i}}{\lambda_{u_1} + \lambda_{u_2} + \lambda_{u_3}}. \tag{45}$$

Once the three eigenvalues of R_{ij} are determined, it is possible to obtain the corresponding eigenvectors from the solution of the equations:

$$\left(\lambda_{u_k}\delta_{ij} - R_{ij}\right)x_k = 0, \tag{46}$$

where λ_{u_k}, $k = \{1,2,3\}$ represent the three eigenvalues of R_{ij}.

The eigenvectors obtained by the solution of Equation (46) are invariant with respect to addition or multiplication by a constant. Therefore, the eigenvectors of R_{ij} and b_{ij} are the same.

The Lumley triangle graphically exhibits the states of realizable turbulence in terms of the invariants (Π_b and III_b) or eigenvalues (η and ξ) of b_{ij}:

$$II_b = -3\eta^2 = -\left(\lambda_{b_1}^2 + \lambda_{b_1}\lambda_{b_2} + \lambda_{b_2}^2\right), \quad (47a)$$

$$III_b = 2\xi^3 = -\lambda_{b_1}\lambda_{b_2}\left(\lambda_{b_1} + \lambda_{b_2}\right), \quad (47b)$$

Figures 10(a) and (b) show the Lumley triangle in terms of (η and ξ) and (Π_b and III_b), respectively. The limiting cases and their physical significance when the invariants/eigenvalues lie on the boundaries of the Lumley triangle are indicated in the figures.

The Reynolds stress ellipsoid is defined by the expected value equation:

$$E(U, \alpha) \leq 1, \quad (48)$$

for given constant $\alpha \geq 0$ with solution given in Equation (49).

$$\left(\frac{U_1 - \overline{U_1}}{\alpha\sqrt{\lambda_{u_1}}}\right)^2 + \left(\frac{U_2 - \overline{U_2}}{\alpha\sqrt{\lambda_{u_2}}}\right)^2 + \left(\frac{U_3 - \overline{U_3}}{\alpha\sqrt{\lambda_{u_3}}}\right)^2 \leq 1, \quad (49)$$

Equation (49) represents an ellipsoid centered at $\left(\overline{U_1}, \overline{U_2}, \overline{U_3}\right)$ with the half-lengths of the principal axes being $\alpha\sqrt{\lambda_{u_i}}$, $i = (1,2,3)$, where $\alpha = 1$ will be assumed, such that Equation (49) represents the surface of the ellipsoid. Therefore, the ellipsoid represents the volume in velocity space of the realizable fluctuations of the turbulence at the vortex core.

Discussion

Figures 11 and 12 provide the R_{ij} and b_{ij} values for the 4DPTV, TPIV, and DES, using bar chart representations. The 4DPTV exhibits larger values for all three normal stresses compared to TPIV and DES. On the other hand, the DES displays the smallest values for $\overline{uu}$, $\overline{vv}$ and $\overline{ww}$. Consequently, the turbulent kinetic energy of the 4DPTV is approximately three times larger than that of the DES.

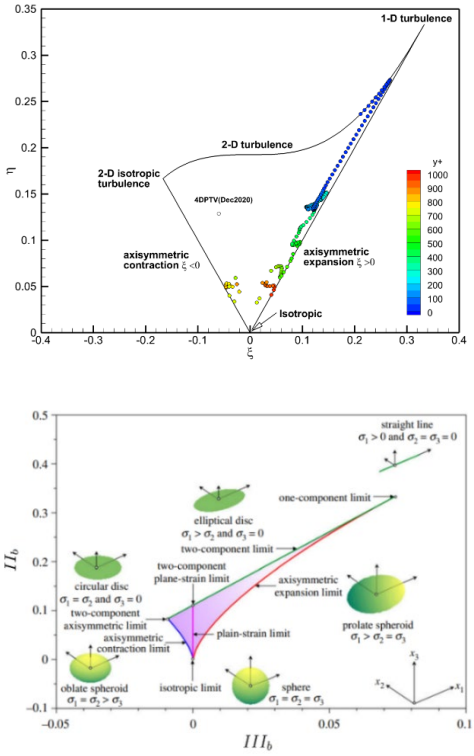

Figure 10: (a) Lumley triangle (Muthu and Bhushan, 2020) and (b) anisotropic invariant map (Subhasiah et al.,2020), σ_i represents the Reynolds stress tensor eigenvalues.

The trend for $\overline{uv}$ and $\overline{uw}$ is similar among all three methods, with differences in magnitude. DES shows the opposite sign compared to 4DPTV and TPIV for $\overline{vw}$. The normal components of b_{ij} show that DES, 4DPTV, and TPIV have the largest values for b_{11}, b_{22}, b_{33}, respectively. It is important to notice that b_{22} for TPIV and DES shows the opposite sign compared to the 4DPTV; 4DPTV shows the largest value for b_{12}, whereas DES for b_{13}. DES also shows the opposite sign for b_{23} compared to the 4DPTV and TPIV. The components of R_{ij} and b_{ij} are related to their eigenvalues by the non-linear system shown in Equations (42)-(44). It is not trivial to understand the contribution of each element of the Reynolds stress tensor in the anisotropy. However, the magnitudes of the normal stresses are much larger compared to the shear stress terms, which could indicate that they play a dominant role in determining the eigenvalues and potentially the eigenvectors of the Reynolds stress tensor.

Table 5 provides R_{ij} and b_{ij} eigenvectors (direction cosines) for the 4DPTV, TPIV, and DES; and Figures 13 and 14 provide their eigenvalues via

bar chart representations. The eigenvalues of the Reynolds stress are ordered in descending order, i.e., λ_{u_1} is the largest. The 4DPTV exhibits the largest eigenvalues for R_{ij}, followed by the TPIV, and DES. Since the trace of a tensor is an invariant, the sum of the Reynolds stress eigenvalues must be equal to two times the turbulent kinetic energy. Note that while λ_{u_1} is the largest eigenvalue for the Reynolds stress, the eigenvalues of b_{ij} are not ordered in descending order but given by Equation (45). Largest values for λ_{b_2} and λ_{b_3} are for the DES, whereas the TPIV exhibits the maximum λ_{b_1}. The sign of λ_{b_2} is negative for TPIV and DES and positive for 4DPTV. This fact has important consequences for the location of the turbulence in the Lumley triangle, as will be shown later.

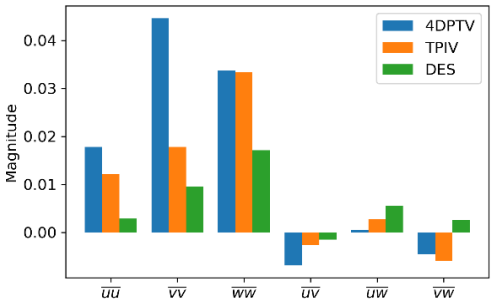

Figure 11: Comparison of Reynolds stress components: 4DPTV, TPIV, and DES.

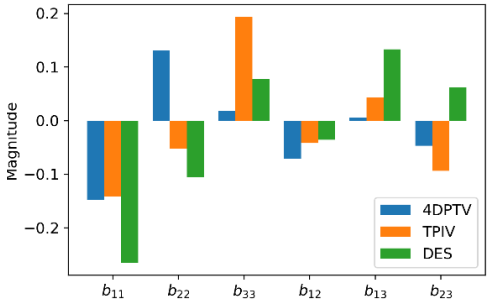

Figure 12: Comparison of anisotropic Reynolds stress components: 4DPTV, TPIV, and DES.

Based on the eigenvalues of b_{ij}, the invariants of the turbulence are evaluated and represented on the Lumley triangle and Anisotropic Invariant Map (AIM) in Figures 15(a) and (b), respectively. The 4DPTV shows a negative value for $\xi\ (III_b)$, whereas this quantity is positive for both the DES and TPIV. The magnitude of $\eta\ (-\Pi_b)$ is largest for the DES, and almost two times larger than the TPIV and 4DPTV. DES predicts a turbulence state very close to the two-component limit, whereas the 4DPTV is closer to an axisymmetric contraction. For the TPIV and DES, the change of sign in λ_{b_2} determines a positive value for $\xi\ (III_b)$. Consequently, for the TPIV the turbulence state is almost on the right border of the Lumley triangle, corresponding to an axisymmetric expansion.

Table 5: Reynolds Stress and Anisotropic Reynolds Stress Tensor Eigenvectors for 4DPTV, TPIV, and DES.

	4DPTV	TPIV	DES
x_{R_1}	$\begin{Bmatrix}0.219\\-0.927\\0.306\end{Bmatrix}$	$\begin{Bmatrix}0.143\\-0.329\\0.934\end{Bmatrix}$	$\begin{Bmatrix}0.295\\0.199\\0.935\end{Bmatrix}$
x_{R_2}	$\begin{Bmatrix}-0.103\\0.290\\0.951\end{Bmatrix}$	$\begin{Bmatrix}-0.326\\0.875\\0.358\end{Bmatrix}$	$\begin{Bmatrix}0.297\\-0.949\\0.109\end{Bmatrix}$
x_{R_3}	$\begin{Bmatrix}0.970\\0.240\\0.032\end{Bmatrix}$	$\begin{Bmatrix}0.934\\0.356\\0.358\end{Bmatrix}$	$\begin{Bmatrix}0.908\\0.245\\0.109\end{Bmatrix}$

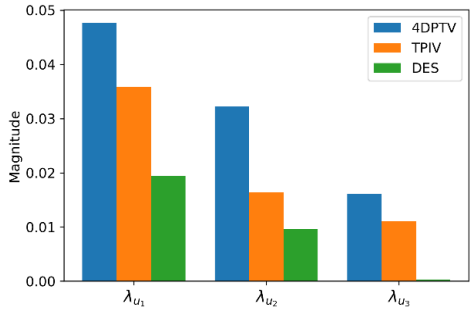

Figure 13: Comparison of Reynolds stress eigenvalues: 4DPTV, TPIV, and DES.

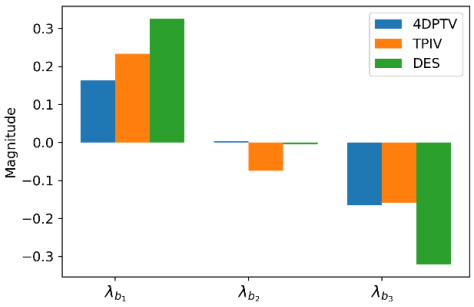

Figure 14: Comparison of anisotropic Reynolds stress eigenvalues: 4DPTV, TPIV, and DES.

The corresponding shapes of the Reynolds stress ellipsoid for the 4DPTV, TPIV, and DES are shown in Figures 16(a), (b) and (c), respectively. For the 4DPTV, $\sqrt{\lambda_{u_1}}$~1.2$\sqrt{\lambda_{u_2}}$~1.7$\sqrt{\lambda_{u_3}}$ implies that the semi-axes in the x_{R_1} and x_{R_2} directions are very close in magnitude, whereas the third direction is

almost half in length. This confirms that the shape of the ellipsoid is close to an oblate spheroid, where $\sqrt{\lambda_{u_1}} = \sqrt{\lambda_{u_2}} > \sqrt{\lambda_{u_3}}$. For the TPIV, $\sqrt{\lambda_{u_1}} \sim 1.5\sqrt{\lambda_{u_2}} \sim 1.8\sqrt{\lambda_{u_3}}$ such that the semi-axis in the x_{R_1} direction is larger than the other two directions. In this case, the ellipsoid resembles a prolate spheroid, where $\sqrt{\lambda_{u_1}} > \sqrt{\lambda_{u_2}} = \sqrt{\lambda_{u_3}}$. DES exhibits a more flattened shape, with $\sqrt{\lambda_{u_1}} \sim 1.4\sqrt{\lambda_{u_2}} \sim 7.4\sqrt{\lambda_{u_3}}$ and the ellipsoid collapses into an almost 2D elliptical disc, where $\sqrt{\lambda_{u_1}} > \sqrt{\lambda_{u_2}}$ and $\sqrt{\lambda_{u_3}} = 0$. This characteristic shape is typical of 2D turbulence. The principal axis associated with the largest eigenvalue indicates the direction where the velocity fluctuations are most pronounced. For the 4DPTV, this almost coincides with the second component of the velocity (V), whereas both the TPIV and DES exhibit a predominant alignment with the third component (W).

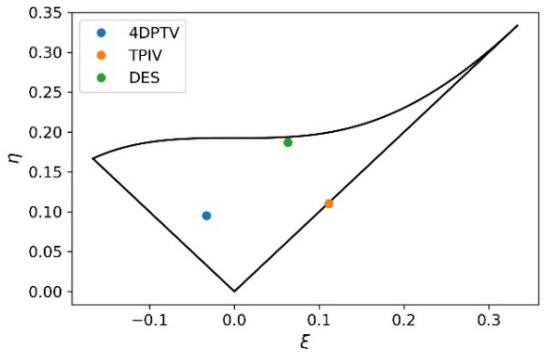

(a)

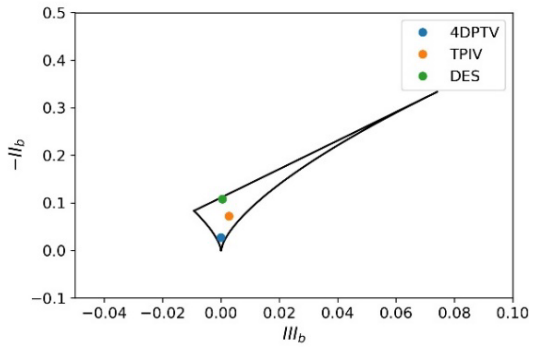

(b)

Figure 15: (a) Lumley and (b) anisotropic invariant map with 4DPTV, TPIV, and DES realizations.

Similarly, the normal stresses for the 4DPTV show that $\overline{vv}$ is the largest, whereas for the TPIV and DES $\overline{ww}$ is the dominant term. Hence, it is postulated that the normal stresses play an important role in determining the principal axes for the Reynolds stress ellipsoid.

For the 4DPTV and TPIV, the principal axis associated with the largest eigenvalue is nearly perpendicular to the direction of the mean velocity vector, as shown in Table 6 and Figure 16. This indicates that the maximum fluctuations of the velocity vector occur in a plane that is perpendicular to the mean velocity direction. In the case of the DES, the angle is around 71 deg. More generally, the plane generated by $x_{\mathcal{R}_1}$ and $x_{\mathcal{R}_2}$ is almost perpendicular to the velocity vector, such that the angle between $x_{\mathcal{R}_3}$ and $\overline{U}$ is less than 10 deg for the 4DPTV and TPIV, and 20 deg for DES. Consequently, the fluctuations of the instantaneous velocity mostly happen on the plane perpendicular to the mean velocity and vorticity vectors. Therefore, the turbulence, which is strongest at the vortex core, is diffused almost perpendicular to its axis.

Conclusions

The Reynolds stress tensor and its normalized anisotropic counterpart, the anisotropic Reynolds stress tensor, offer a comprehensive description of turbulence in terms of its normal stresses and anisotropy. The 4DPTV shows much larger normal stresses, resulting in a large magnitude of the turbulent kinetic energy compared to the TPIV and DES. The eigenvalues and eigenvectors of these tensors help identify the principal directions and magnitudes of the turbulent fluctuations. In particular, the analysis of the Lumley triangle or AIM further visualizes the different states of turbulence based on the invariants of the anisotropic Reynolds stress tensor.

The shape of the Reynolds stress ellipsoid, determined by the eigenvalues, reflects the volume of realizable fluctuations in velocity space. The 4DPTV, TPIV, and DES reveal very different shapes for the ellipsoids caused by different locations of the turbulence in the Lumley triangle or AIM. DES predicts an almost 2D state of turbulence, such that the characteristic ellipsoid degenerates into an elliptical disc. The turbulence for the 4DPTV and TPIV shows similar magnitudes for the invariants, with the main difference due to the change in sign of λ_{b_2}, which determines a shift towards positive ξ for the TPIV. The dissipation tensor was decomposed into isotropic and anisotropic components (results not shown), which provided insights into the rate of energy dissipation (contributions of the ε_{ij}components to ε)

Table 6: Characteristics of the Reynolds Stress Ellipsoid and its Orientation vs. Mean Velocity and Mean Vorticity Vectors for 4DPTV, TPIV, and DES.

	Semi-axes of the RS ellipsoid			Angle between RS ellipsoid principal axes and $\overline{U}$ [deg]			Angle between RS ellipsoid principal axes and $\overline{\Omega}$ [deg]		
	$\sqrt{\lambda_{u_1}}$	$\sqrt{\lambda_{u_2}}$	$\sqrt{\lambda_{u_3}}$	$x_{\mathcal{R}_1} \cdot \overline{U}$	$x_{\mathcal{R}_2} \cdot \overline{U}$	$x_{\mathcal{R}_3} \cdot \overline{U}$	$x_{\mathcal{R}_1} \cdot \overline{\Omega}$	$x_{\mathcal{R}_2} \cdot \overline{\Omega}$	$x_{\mathcal{R}_3} \cdot \overline{\Omega}$
4DPTV	0.219	0.180	0.127	91.14	98.07	8.13	99.63	96.37	11.57
TPIV	0.189	0.128	0.105	93.81	95.60	6.02	94.28	90.49	4.33
DES	0.139	0.098	0.019	70.80	73.13	26.01	73.99	87.10	16.28

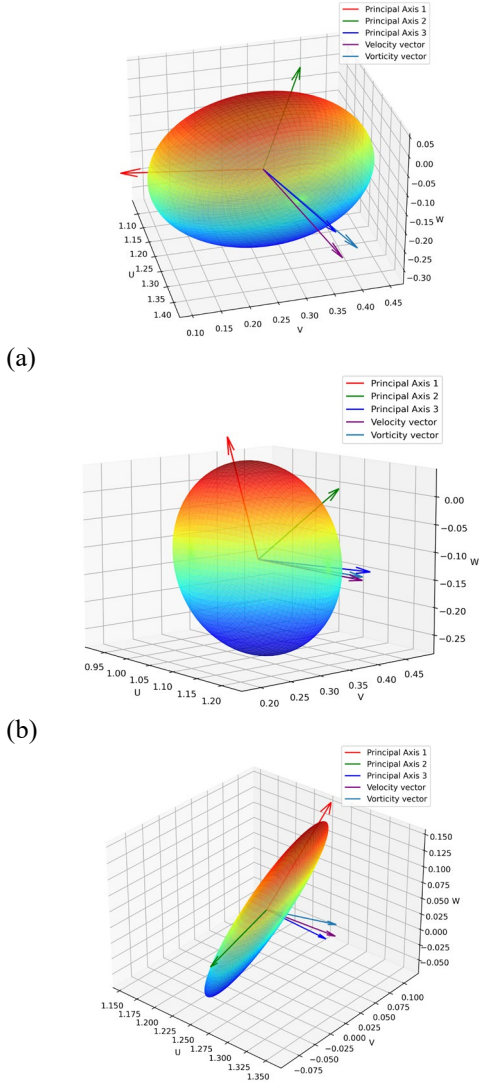

(a)

(b)

(c)

Figure 16: Reynolds stress ellipsoids; (a) 4DPTV, (b) TPIV, and (c) DES. The velocity and vorticity vectors are scaled by their magnitude multiplied by a constant.

and its anisotropic behavior and it was analyzed only for the 4DPTV. While the normal components show similar trends when compared between $\varepsilon_{ij}(\widetilde{\varepsilon_{ij}^{A}})$ and $R_{ij}(b_{ij})$, no conclusions could be drawn for the off-diagonal components.

Overall, these analyses reveal the distinct characteristics of turbulence captured by different measurement techniques such as 4DPTV and TPIV and the DES, highlighting their strengths and limitations in characterizing turbulent flow.

Future research will focus on conducting a sensitivity analysis study for the relationship presented in Equations (42)-(44), which connects the invariants of b_{ij} with the components of the Reynolds stresses. This analysis will provide additional insights into the dominant components influencing the determination of the turbulence state, as indicated by the Lumley triangle, and will help understand the differences between the 4DPTV, TPIV, and DES. The anisotropy results will be compared with the isotropic eddy viscosity concept using the mean rate of strain.

VORTEX BREAKDOWN AND INTERACTION

Xing et al. (2012) identified spiral vortex breakdown followed by helical mode instability in their DES for KVLCC2 at β = 30 deg and its analogy with delta wing flows; however, experimental validation is still not available for KVLCC2. The evidence for this was the transition of the vortex core streamlines from straight to helical, the nature of the variation of the vortex core variables (i.e., increase in TKE and p and decrease in u and ω_x), and the same scaling for the vortex core Strouhal numbers based on ship length (L) ($St = fL/U$ and $St_{D_S} = fD_S/U$) as delta wings. For ship flows the transition was without an abrupt increase in vortex size, and less prominent and/or differences in the nature of the vortex core variables, which was attributed to the fact that for ship flows the vortices are embedded in the hull boundary layer. Bhushan et al. (2019, 2021) DES for 5415 at β = 20 deg showed similar vortex breakdown characteristic as KVLCC2 and this time with TPIV validation for St and St_{D_S}. It should be noted that ship flow geometries and separation types are mostly different

than delta wings, i.e., smooth surfaces with crossflow and bubble type separations vs. sharp edges with sharp edge separations for delta wings, except for bilge keels and other similar appendages with sharp edges.

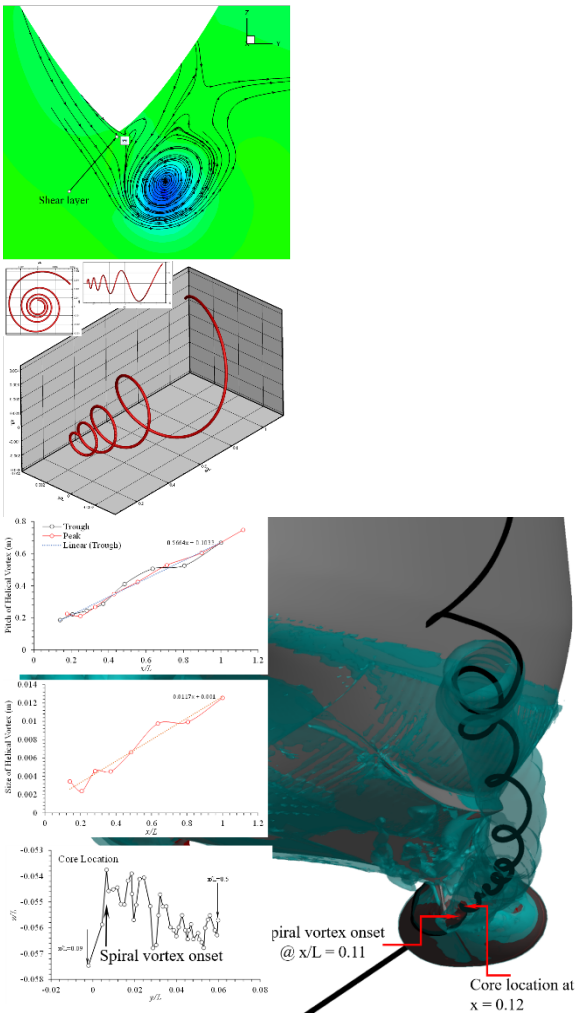

Figure 17: Planar streamlines at x/L = 0.12 showing the spiral vortex (upper left); model for the helical path of the vortex core from x/L = 0.11 to x/L = 1 (upper right); and helical instability emerging from the spiral vortex breakdown at x/L = 0.11, including inserted plots showing the pitch of the helix, size of the helix, and helix core locations (lower).

Figure 17 provides improved analysis of the DES vortex breakdown/helical mode instability. Figure 17 (top left) shows planar streamlines at x/L = 0.12. The flow spirals inwards towards the vortex core. The shear layer due to the crossflow around the keel wraps around the vortex core. Figure 17 (bottom) shows the upstream streamline that merges into and emerges from the vortex core at x/L = 0.12. The vortex core is identified by the high Q =10000 value iso surface (red). The transparent iso surface in blue is for Q = 100, which shows the primary vortex structure. The top inset plot shows the pitch of the helical vortex. The pitch increases linearly with progression with values of around 0.2 m at onset to 0.75 m aft of the stern. The middle-inset plot shows the estimated size of the helical vortex, which also increases linearly with distance from onset. The bottom inset plot shows the vortex core location that was manually extracted from the peak Q values at slices of x/L = 0.09 to 0.5 at every 0.01L. The vortex core shows an upwards drift between x/L = 0.09 to 0.11, and then shows unsteady helical motion. Figure 17 (top right) shows a model for the helical path of the vortex core from x/L = 0.11 to x/L = 1. The inset plots show the view of the helical path in the y-z and x-z planes. The helical path is obtained using the equation $y/L = A(x/L)\sin(\omega(x/L) \times x/L)$ and $z/L = A(x/L)\sin(\omega(x/L) \times x/L)$. The frequency $\omega(x/L)$ is estimated from the pitch of the helical vortex, which gives $\omega(x/L) = 2\pi L/(0.1 + 0.5664x)$. The amplitude is estimated from the size of the helical vortex, which gives $A(x/L) = (0.001 + 0.0117x)/L$.

Clearly the streamlines in the SDVP vortex undergo transition from straight to helical with the spiral vortex breakdown estimated to occur at about x/L = .11. The wavelength of the $u(x,t)$ spatial waves and pitch of the helix vortex core at x/L = 0.12 closely agree. The linear growth for the helix pitch indicates the same frequency scaling as shown previously for KVLCC2 and 5415, as per Figure 5(e).

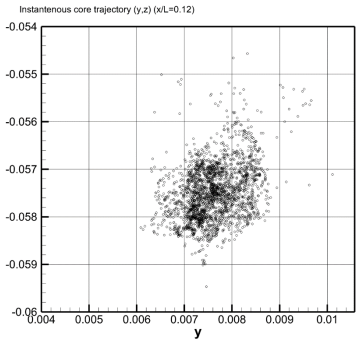

Figure 18: Instantaneous SDVP vortex core (y, z) trajectory at x/L = 0.12.

Figure 18 shows the instantaneous trajectory in the (y, z) plane at x/L = 0.12. The FFT of the SDVP at x/L = 0.12 core coordinates and displacement velocity were compared with the FFT of u. All three

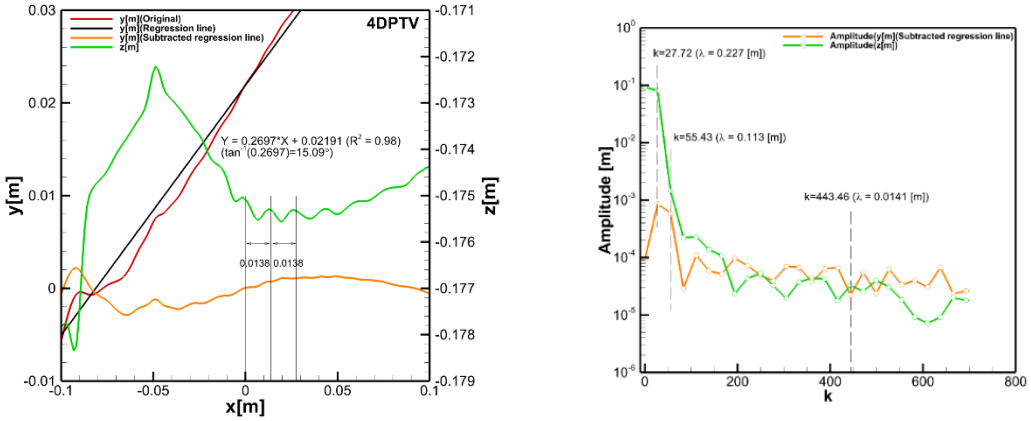

(a)

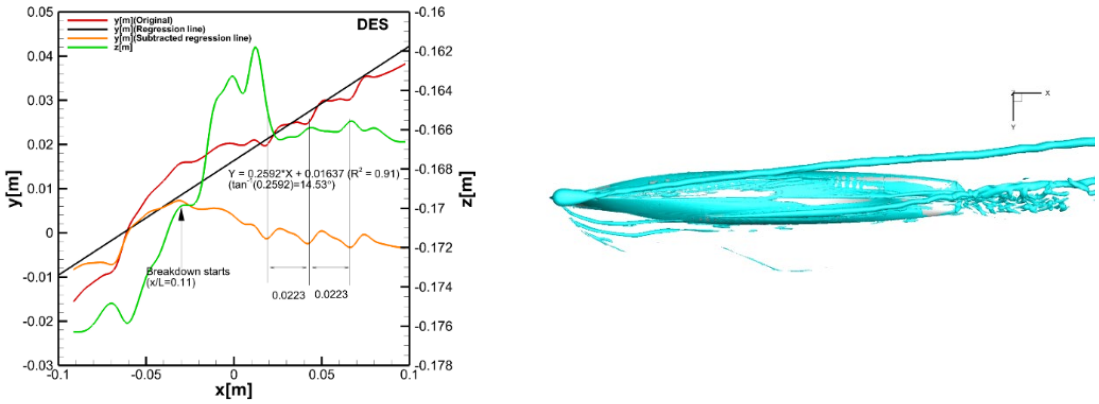

(b)

Figure 19: 4DPTV streamwise vortex core (y, z) trajectory coordinates and FFT (a); and DES streamwise vortex core (y, z) trajectory coordinates and global view of the SDVP vortex (b).

variables show similar behavior. Thus, the turbulent axial velocity and vortex core displacement and velocity all show the footprint of the spiral vortex breakdown/helical mode instability.

Figure 19 shows the 4DPTV streamwise vortex core (y, z) trajectory coordinates and FFT (a) and DES streamwise vortex core (y, z) trajectory coordinates and global view of the SDVP vortex (b). The SDVP y coordinate trajectory is in line with the drift angle β = 10 deg with somewhat larger values near its onset. The streamwise vortex core (y, z) trajectories show low-frequency oscillations that correspond to the spiral vortex breakdown/helical mode instability and high-frequency oscillations that correspond to those shown in the spatial autocorrelation Figure 6(b, c). Sanada et al. (2023) figures 20 through 30 show what appear to be shear layer vortices covering the surface of both the SDVP and SDVS vortices with wave lengths like those shown in the streamwise vortex core (y, z) trajectories. It is hypothesized that the high frequency oscillations of the streamwise vortex core (y, z) trajectories are due to the shear layer that wraps around the spiral vortices as per Figure 17 (upper left) and its associated Kelvin-Helmholtz instability. However, it should be recognized that the resolution of the shear layer vortices and the Kelvin-Helmholtz instability is at the limit of the current 4DPTV resolution, and as is also the case with resolving the Taylor microscale, increased resolution is required. Based on figures 18 and 19, the SDVP wandering is due both to the spiral vortex breakdown/helical mode instability and the shear layer vortices.

The 5415 β= 10 deg 4DPTV and DES clearly show that the SDVP vortex undergoes spiral vortex breakdown/helical mode instability with many features like the delta wing spiral vortex breakdown/helical mode instability. The swirl numbers are lower than expected based on the vortex

breakdowns for delta wings and swirling jets and pipe flows; however, SDVP undergoes strong interaction with SDVS such that it is hypothesized that this interaction induces the vortex breakdown. Leweke (2016) shows that corotating vortex pairs are susceptible to shortwave instabilities produced by the strain induced from one vortex to the other. Further research is ongoing.

CONCLUSIONS AND FUTURE RESEARCH

Additional analysis of the 4DPTV static drift β = 10 deg results for the 5415 sonar dome vortices is made to realize its full potential for the assessment of the turbulence structure and vortex breakdown and interactions and for providing data for scale resolved CFD validation. Limitations of the current 4DPTV system are identified for future improvements. The 4DPTV has increased capability compared to the previous TPIV in terms of measurement volume size and sampling rate, whereas it has less spatial resolution. The assessment includes comparisons with both the previous TPIV and DES. The focus is on the strongest primary vortex SDVP at x/L = 0.12 (just downstream of the sonar dome) and its interaction with SDVS, which is the second strongest of the multiple sonar dome vortices. Both vortices are counterclockwise and due to cross flow separations with SDVP and SDVS onset from the windward (port) and leeward (starboard) sides of the sonar dome.

The macro-scale analysis showed agreement between 4DPTV and TPIV for the SDVP elliptically shaped cross plane streamlines and Gaussian and Bell distribution for the axial vorticity and Q-criteria. The macro-scale turbulence is larger for the 4DPTV vs. the TPIV, whereas the vortex strength has the opposite trend, and the anisotropy shows both similarities and differences. The DES shows similar trends as the experiments, but there are large quantitative differences.

The micro-scale analysis used model spectrums based on the 4DPTV and TPIV macro-scales, as benchmarks which were about half the size of their spatial resolutions and indicates that sub-millimeter resolution is needed to resolve the micro-scales accurately. The temporal and spatial autocorrelation functions were used to compute the micro-scales. The Taylor micro-scales (λ_f) were consistently larger than their benchmarks and roughly twice their spatial resolutions. The larger λ_f resulted in the dissipation ε being significantly smaller than the benchmark. The η values were larger than the benchmark, but the difference with the benchmark were not as large as that for the λ_f. The temporal 4DPTV analysis resolved the energy containing range and a large portion of the inertial sub range of the turbulence. The spatial 4DPTV analysis resolved a narrower band compared to the temporal analysis, and primarily resolved the inertial subrange.

The anisotropy analysis of the 4DPTV, TPIV, and DES showed similarities and distinct differences between the three results which highlights the strengths and limitations for characterizing the turbulence structure. The DES predicts an almost 2D turbulence state whereas the 4DPTV and TPIV display Reynolds stress ellipsoids that resemble oblate and prolate spheroids, respectively. The analysis of the Reynolds stress ellipsoids suggests that the principal axes are largely affected by the differences in the normal components of the Reynolds stresses; however, sensitivity analysis is needed to confirm this postulation.

The 4DPTV measurements and DES provide strong evidence that SDVP undergoes a spiral vortex breakdown/helical mode instability like KVLCC2 and 5415 at static drift β = 30 and 20 deg, respectively, and delta wings. The SDVS vortex is shed periodically with visually evident interactions between SDVP and SDVS, which suggests that such vortex interactions induce the SDVP spiral vortex breakdown/helical mode instability at smaller swirl numbers than what is observed for other flows without such interactions.

Future research will focus on additional anisotropy analysis, including more points along a radial line perpendicular to the vortex core and along the vortex core upstream and downstream of x/L = 0.12, for a more global determination of the turbulence state and for evaluation of the eddy viscosity concept. The vortex interactions will be investigated in more detail. FFT analysis is needed to determine the period and wavelength of the SDVP and SDVS vortex cores and the SDVS vortex shedding, and a triple-decomposition could be leveraged to remove the oscillation of the spiral vortex breakdown/helical mode instability for further temporal turbulence analysis. The interactions between SDVS and SDVP are complex, and future analysis will be done to determine the mechanism of the merging of SDVS and SDVP. To accomplish this, simultaneous and instantaneous vortex core tracking must be done for both SDVP and SDVS and distances between their cores must be evaluated over the entire measurement range and duration. Also, TKE budget analysis needs to be done for both SDVP and SDVS for better

understanding their progressions and interactions, which requires evaluation of the pressure transport term.

ACKNOWLEDGEMENTS

This research was sponsored by the Office of Naval Research under grants N00014-21-1-2060, N00014-21-1-2399, and N00014-22-1-2597 under the administration of Dr. Woei-Min Lin. Dr. Zhaoyuan Wang contributed to the derivations.

REFERENCES

Banerjee, S., Krahl, R., Durst F. and Zenger, C., "Presentation of Anisotropy Properties of Turbulence, Invariants versus Eigenvalue Approaches," Journal of Turbulence, Vol.8(32), 2007, DOI:10.1080/14685240701506896

Bernard, P.S., Turbulent Fluid Flow, John Wiley & Sons, Inc, 2019

Bhushan, S., Yoon, H., Stern, F., Guilmineau, E., Visonneau, M., Toxopeus, S., Simonsen, C., Aram, S., Kim, S.-E. and Grigoropoulos, G., "Assessment of CFD for Surface Combatant 5415 at Straight Ahead and Static Drift β=20 deg," Journal of Fluids Engineering, Vol. 141(5), 2019, 051101.

Bhushan, S., Yoon, H., and Stern, F., "Detached Eddy Simulations and Tomographic PIV Measurements of Flows over Surface Combatant 5415 at Straight-Ahead and Static Drift Conditions," Ocean Engineering, Vol. 238, 2021, 109658.

Dey, S., Prianka, P., Ali, S. and Padhi, E., "Reynolds Stress Anisotropy in Flow over Two-dimensional Rigid Dunes," Proceedings of the Royal Society A: Mathematical, Physical and Engineering Sciences, Vo.476, 2020, 20200638. 10.1098/rspa.2020.0638.

Greenwell, D. I., "Chapter 21 - Engineering Models of Delta Wing Vortex Breakdown and Its Effect on Aerodynamic Characteristics," STO Technical Report RTO-TR-AVT-080, 2009.

Gursul, I., "Chapter 6 – Unsteady Aspects of Leading-Edge Vortices," STO Technical Report RTO-TR-AVT-080, 2009.

Hino, T., Stern, F., Larsson, L., Visonneau, M. Hirata, N. and Kim, J. (editors), Numerical Ship Hydrodynamics: An Assessment of the Tokyo 2015 Workshop, Springer, 2020.

Leweke, T., Le Dizès, S., Williamson, C., "Dynamics and Instabilities of Vortex Pairs," Annual Review of Fluid Mechanics, Vol. 48, 2016, pp.507-541.

Muthu, S. and Bhushan, S., "Comparison between temporal and spatial direct numerical simulations for bypass transition flows," Journal of Turbulence, Vol.21(5-6), 2020, pp.311-354.

NATO STO, "Reliable Prediction of Separated Flow Onset and Progression for Air and Sea Vehicles," STO Technical Report TR-AVT-183, 2017.

NATO STO, "Assessment of Prediction Methods for Large Amplitude Dynamic Maneuvers for Naval Vehicles," STO Technical Report TR-AVT-253, 2021.

Pope, S.B., Turbulent Flows, Cambridge Univ. Press, 2000.

Sanada, Y., Starman, Z., Bhushan, S., and Stern, F., "Four-dimensional particle tracking velocimetry measurements of unsteady 3D vortex onset and progress for 5415 straight ahead, static drift and pure sway," Physics of Fluids, Vol. 35(10), 2023, 105125. https://doi.org/10.1063/5.0165658.

Schumann, U., "Realizability of Reynolds-stress turbulence models," Physics of Fluids, Vol.20 (5), 1977, pp.721–725.

Stern, F., Milano, C., and Wang, Z., http://user.engineering.uiowa.edu/~me_7268/TurbulentFlow_main.htm, 2023.

Yoon, H. and Stern, F., "Phase-averaged TPIV Measurements for Surface Combatant 5415 in Pure Sway Maneuver: Experimental Setup, UA and Preliminary Results," Proceedings of the. 30th American Towing Tank Conference, Oct. 2017, Bethesda, MD, USA.

Xing, T., Bhushan, S., Stern, F., "Vortical and turbulent structures for KVLCC2 at drift angle 0, 12, and 30 degrees," Ocean Engineering, Vol. 55, 2012, pp.23–43.

DISCUSSION 1 (D1)

Charles Meneveau, Department of Mechanical Engineering, Johns Hopkins University

The paper is an excellent example of best practices of a joint experimental and computational data analysis in an interesting, highly complex flow of direct naval interest. The experimental resolution and that of the computations are approximately matched, focusing on large and intermediate scales rather than microscales. The computational (DES) data were obtained some time ago and the fact that they can still be used productively is definitely a plus.

1. The comparison of spectra is of interest since both experimental data and DES are "eddy resolving". For directly obtained spectra (even for the DES data where signals are probably shorter duration) one recommendation would be to use averaging to obtain less noisy experimental spectra (e.g., Fig 7,8). It is OK to forego resolving the lowest-frequency modes and average over (e.g.) 10 or 20 windowed segments of the signal. For spectra obtained from FT of the correlation function, perhaps first fitting the latter with a smooth function, and then doing the FT would reduce the large amount of noise visible in the spectra. Such large noise makes comparisons between simulation and experiments more difficult. Certainly, the use of model spectra to complete the unmeasured small scales is a good approach.

2. The observations regarding vortex structures, anisotropy and characteristic length scales all contribute to a solid and important database for future simulations to compare with. The conclusions summarize the benchmark values methodically, which will be helpful for further follow-up studies.

3. In the conclusions when discussing the start of the dissipation range, the authors state "...dissipation range is established at 60η, based on Kolmogorov's hypothesis of local isotropy". It was unclear to me how the Kolm-local isotropy hypothesis can be used to identify this range limit. Why not 40 eta or 50 eta?

4. Figure 2 caption needs to state what (c) is (I assume it is DES).

5. As an overall conclusion and discussion topic, it appears that while the experiments and simulations provide similar trends, there are significant quantitative differences. What are the implications of the observed level of differences? The differences appear a bit larger than the differences among the two measurement methods (4DPTV and TPIV), but the latter also differ by quite a bit. How should such observations affect future LES/DES model developments and experimental tools?

AUTHOR'S REPLY

Thank you for your positive and helpful comments.

Comment 1: We appreciate that you found our comparison of spectra of interest. We hope you also find our evaluation of the Taylor micro and macro scales of equal interest, as in our field especially for practical geometries both spectral and especially Talyor scale analysis are seldom done. Your comment resulted in our reinvestigating our spectra and Taylor macro and micro scale estimates. In doing so we have preferred to use $L = l_0$ in the analysis, as explained in the text. Also, we found a minor error in our data reduction for the spectral and Talyor scale analysis, which we have corrected and explained below. In summary, we find upon taking into consideration aliasing and the Nyquist criteria that the best approach is the use of a Butterworth filter, which leads to the most reasonable results for both the temporal and spatial analysis; however, in the latter case the results are less satisfactory, as they are much more sensitive to our coarse spatial resolution. Lastly and in our opinion most importantly our reinvestigation has led to the following hypothesis: to achieve proper resolution of the energy containing range macro scales, turbulence anisotropy and organized oscillations it is necessary to simultaneously resolve both the temporal and spatial Taylor micro (λ_f) and macro (Λ_f) scales in experiments and/or simulations. The discussion that follows is organized to explain our new results in support of this hypothesis.

Evidence

1. The high frequency/large wave number tail of the energy spectrums shown in the 5415 primary sonar-dome vortex SDVP core 4DPTV measurements both without (Stern et al. 2024) and with the use of a moving average (MA) filter (Sanada et al. 2023)[2] display anomalous behavior, which is attributed to aliasing due to the mismatch of the 4DPTV temporal (444.2 Hz) and spatial (2.1 – 4.2 mm) resolutions.
2. The λ_f and Λ_f values for the MA filtered data are about five times larger than for the unfiltered data. The unfiltered data λ_f value is on the order of the 4DPTV spatial resolution, which is about 3 times larger than the expected benchmark value, i.e., about 1 - 2 mm. Whereas the Λ_f values for the filtered vs. unfiltered data are likely too small vs. unreasonably too large.
3. The turbulence in the SDVP core is shown to be transported by the mean flow such that the Taylor Frozen Turbulence Hypothesis (TFTH) is valid (Stern et al. 2024), which suggest that the proper time interval for data reduction to prevent aliasing should be determined by $\Delta t = \Delta x/\langle U \rangle$ where Δt is the temporal resolution (444.2 Hz), Δx is the spatial resolution (4.277E-03 m), and $\langle U \rangle$ (1.248 m/s) is the mean velocity. Therefore, the frequencies that exceed $f = 1/\Delta t$ (291.8 Hz) should be excluded via use of filtering, which is also consistent with the use of a Nyquist sampling cutoff frequency criteria.
4. Results shown below with the use of a Butterworth filter with the TFTH (sampling rate 291.8 Hz) and Nyquist cutoff frequency, i.e., f_c = 291.8/2 = 145.9 Hz based on the above reasoning [vs. 222.1 if the Nyquist criteria is used with original sampling rate 444.2 Hz and consistent with some authors (e.g., Bendat and Piersol, 1986) that advocate the use of 50-80% of the Nyquist value for the improvement of the spectrum in the inertial subrange] provide reasonable values for both λ_f and Λ_f, i.e., the former on the order of the spatial resolution and the latter on the order of the vortex half width.

Conclusions

Increased spatial resolution of the 4DPTV measurement system to properly resolve the Taylor micro scale and prevent aliasing will also provide confidence in the proper resolution of the energy containing range macro scales, turbulence anisotropy and organized oscillations, which is the primary focus for the physical understanding of 3D vortex separation onset and progression for flows of practical interest such as the 5415 sonar dome vortices.

Clearly the high frequency data resolution/data reduction influences the low frequency data resolution/data reduction. The use of the Butterworth filter is helpful, but surely accurate resolution of the Taylor micro scale λ_f is required to have confidence that the Taylor macro scale Λ_f and other macro scale features are accurately resolved. The Kolmogorov hypotheses and scaling along with the Richardson cascade concept indicates that the small scales loose memory of the large scales; however, the small scales are created/driven by the large scales such that a balance exists between the large-scale motions/energy containing range and the dissipation/small scale motions, i.e., Λ_f and λ_f are inextricably connected. Thus, achieving the 5/3 power law in the inertial subrange alone does not guarantee that the macro and micro scales are properly resolved and balanced.

Discussion

Table D1-1 shows the macro-scale parameters for the SDVP vortex determined using three different methods: the MA filter (f_c = 7.5 Hz), the unfiltered[3], and the Butterworth filter with TFTH sampling rate and Nyquist criteria (f_c =145.9 Hz). The use of the MA filter weights the large scales and reduces the measured turbulence intensity, dissipation, and Re_L. Assuming $L = l_0$ results in a reduction in Re_L and in the model spectrum benchmark (BM) Taylor micro-scale, as will be shown later. The Butterworth filter

[2] Stern, F., ONR 2023 Hydrodynamics / Structural Acoustics Program Review, 12-16 June, San Diego, CA.

[3] Note that the current unfiltered results show small differences with those in our paper as we found an index error, which is corrected herein. The index error was due to the use of a one voxel outboard value for the mean vortex core location, which highlights the sensitivity of the turbulence to the spatial location. See Tables 5 and 6 below.

values are intermediate between the MA filter and unfiltered results.

Figures D1-1 and D1-2 shows the temporal autocorrelation and its FFT for five different types of time series. (1) unfiltered with sampling rate 444.2 Hz; (2) unfiltered with sampling rate 444.2 Hz reconstructed from the averaged spectrum from all five realizations (towing tank runs) as recommended by Charles Meneveau; the Butterworth filter with sampling rate 444.2 and (3) *fc* = 145.9 Hz and (4) *fc* = 291.8 Hz; and (5) down sampling. Down sampling first uses a *fc* = 145.9 Hz and then samples at 291.8 Hz. The results of (1) and (2) are similar, whereas the results of (3), (4), and (5) are similar and in this case all three remove the high frequency anomalous behavior. Comparing the temporal autocorrelation from the Butterworth-filtered time series with that from the down-sampled time series, both results are well agreed.

The micro-scale parameters are evaluated for the 4DPTV using the same three methods presented above for the macro-scale. The results are compared with the benchmarks, obtained as per Stern et al. (2024) and presented in Tables D1-2 and D1-3. The MA filtered results show unreasonably large Taylor micro and macro scales, with too small dissipation and too large Kolmogorov length scale. The unfiltered results show improvement in both Taylor micro and macro scales, that get closer to the benchmarks. The dissipation increases over two orders of magnitude. Using the Butterworth filter increases both λ_f and Λ_f, with Λ_f approximately equal to half the size of l_0. The Butterworth filter also causes a reduction in the dissipation value. The Butterworth filter results show similar percentage errors with their benchmark, compared to the unfiltered data.

Comment 2: Thank you for your positive and helpful comments.

Comment 3: The start of the dissipation subrange is established using the peak of dissipation spectrum as discussed in Pope (2000) and Bernard (2019). Kolmogorov's hypothesis of local isotropy characterizes the dissipation range scales by a small number of relevant parameters of which the length scale $\eta = (\nu^3/\varepsilon)^{1/4}$ is inversely proportional to the wave number k_d correspondent to the peak of the dissipation spectrum, as shown in Bernard (2019) Figure 4.1. Pope (2000) Figure 6.16 shows that for isotropic decaying turbulence (for $R_\lambda = 600$) the peak of the dissipation spectrum is around $l/\eta \sim 24$ and that the bulk of the dissipation occurs for $60 > l/\eta > 8$. Similarly, experimental studies mentioned by Bernard (2019) show that the peak of the dissipation spectrum is at $k_d \approx \alpha/\eta$ with α =0.1-0.15, or equivalently in terms of length scale $l/\eta \sim 40 - 60$.

The other way to establish the start of dissipation subrange is using Taylor's micro-scale, which represents the largest length-scale that takes part in the dissipation, or the scale when the molecular viscosity starts to play a role. Using the definition of η and $\varepsilon \sim \nu u_{rms}^2/\lambda^2$ one can show that $\lambda/\eta = \sqrt{R_\lambda}$, suggesting that the dissipation subrange is wider for larger R_λ. This is consistent with isotropic decaying turbulence experiments by Kang et al. (2003), wherein λ/η increased from 49 to 53 when R_λ increased from 626 to 716.

The averaged R_λ estimate in this study is 570, thus based on λ/η range above, a reasonable estimate should be $l_{DI} \sim 50\eta$. Therefore $l_{DI} \sim 60\eta$ used in the study represents an upper limit of the demarcation between the inertial and dissipation range.

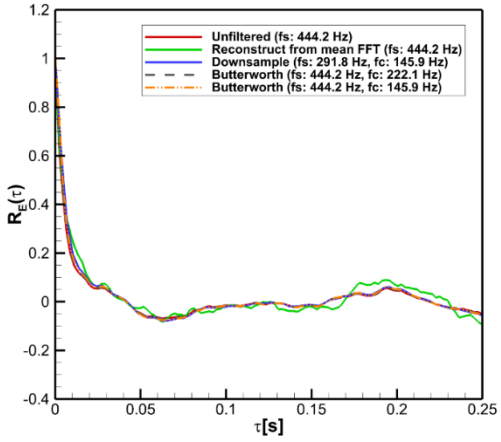

Figure D1-1: Temporal autocorrelation

The primary conclusion at this stage of our temporal analysis is that even though the errors are somewhat larger for the Butterworth filter vs. its BM than the unfiltered vs. its BM the results with the Butterworth filter are deemed the best as they remove the anomalous behavior shown in the high frequency/large wave number tail of the energy spectrum and both BM are only estimates. It is

Table D1-1: Macro-scale parameters using MA filter, unfiltered data (SNH), and Butterworth filter

Parameter	4DPTV					
	SD 2023 MA filter, f_c= 7.5 Hz		SNH 2024, Unfiltered		Butterworth filter, f_c= 145.9 Hz	
	$L = l_0/0.43$	$L = l_0$	$L = l_0/0.43$	$L = l_0$	$L = l_0/0.43$	$L = l_0$
$\langle U \rangle$ [m/s]	1.249	1.249	1.248	1.248	1.248	1.248
$\langle u^2 \rangle$ [m^2/s^2]	0.003	0.003	0.018	0.018	0.016	0.016
k [m^2/s^2]	0.009	0.009	0.048	0.048	0.043	0.043
u_0 [m/s]	0.097	0.097	0.219	0.219	0.207	0.207
l_0 [m]	0.025	0.025	0.025	0.025	0.025	0.025
L [m]	0.058	0.025	0.058	0.025	0.058	0.025
ε [m^2/s^3]	0.016	0.037	0.182	0.422	0.152	0.354
Re_L	4787.3	2058.6	10793.4	4641.2	10148.2	4374.2

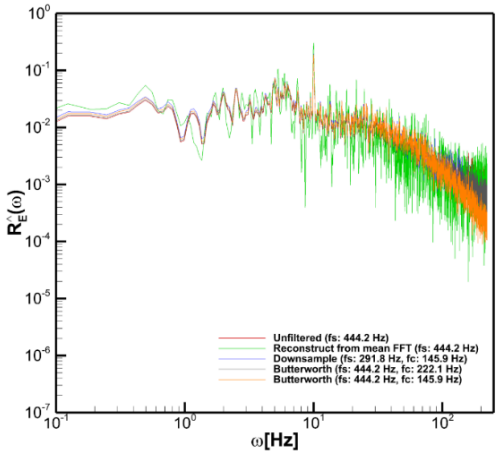

(a) All

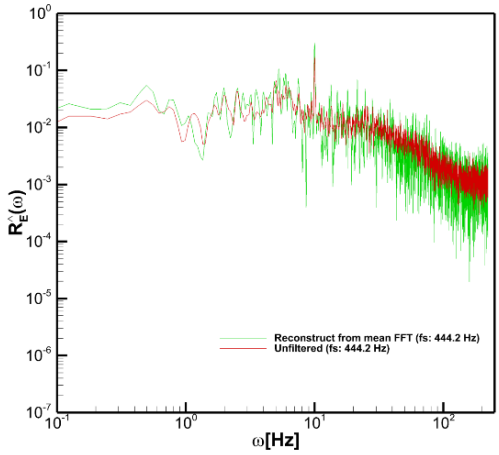

(b) Unfiltered and reconstruct from mean FFT

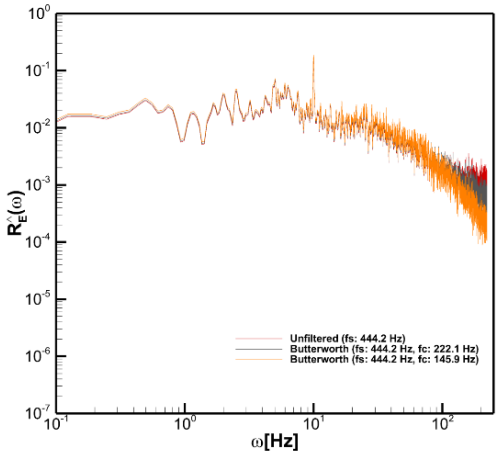

(c) Unfiltered, Butterworth (fc: 222.1 Hz and 145.0 Hz)

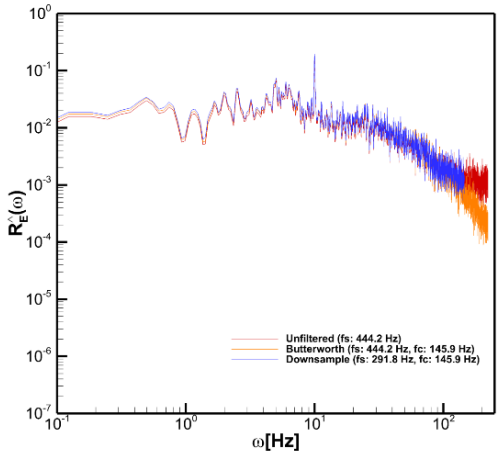

(d) Unfiltered, Butterworth (fc: 145.9 Hz), Downsample (fs: 291.8 Hz, fc: 145.9 Hz)

Figure D1-2: Temporal autocorrelation FFT comparison

Table D1-2: Micro-scale parameters for MA filter and unfiltered data: results and benchmarks.

Parameter	4DPTV BM (MA filter, f_c =7.5 Hz)		Temporal 4DPTV (MA filter, f_c=7.5 Hz)	Temporal 4DPTV (MA filter, f_c =7.5Hz)% 4DPTV BM (MA filter, f_c =7.5Hz, $L = l_0$)	4DPTV BM (unfiltered)		Temporal 4DPTV (SNH 2024, unfiltered)	Temporal 4DPTV (unfiltered) % 4DPTV BM (SNH 2024, unfiltered $L = l_0$)
	$L = l_0/0.43$	$L = l_0$			$L = l_0/0.43$	$L = l_0$		
λ_f [m]	3.76E-03	2.46E-03	2.98E-02	-1109.93%	2.50E-03	1.64E-03	4.64E-03	-182.79%
Λ_f [m]	2.50E-02	2.50E-02	3.52E-02	-40.85%	2.50E-02	2.50E-02	8.01E-03	67.95%
R_λ	1.79E+02	1.17E+02	1.42E+03	-1109.93%	2.68E+02	1.76E+02	4.97E+02	-182.79%
ε [m^2/s^3]	1.58E-02	3.69E-02	2.52E-04	99.32%	1.82E-01	4.22E-01	5.28E-02	87.50%
η [m]	1.01E-04	8.18E-05	2.85E-04	-247.84%	5.49E-05	4.45E-05	7.48E-05	-68.16%

Table D1-3: Micro-scale parameters for Butterworth filter: results and benchmarks.

Parameter	4DPTV BM (Butterworth filter, f_c = 145.9 Hz)		4DPTV (Butterworth filter, f_c = 145.9 Hz)	4DPTV (Butterworth filter, f_c = 145.9 Hz) % 4DPTV BM (Butterworth filter, f_c = 145.9 Hz, $L = l_0$)
	$L = l_0/0.43$	$L = l_0$		
λ_f [m]	2.57E-03	1.69E-03	5.76E-03	-240.75%
Λ_f [m]	2.50E-02	2.50E-02	9.01E-03	63.96%
R_λ	2.60E+02	1.71E+02	5.82E+02	-240.75%
ε [m^2/s^3]	1.52E-01	3.54E-01	3.05E-02	91.39%
η [m]	5.74E-05	4.65E-05	8.58E-05	-84.59%

expected that the Taylor micro scale, once accurately determined, may be equal to or less than about 1 mm.

We also investigated the use of the Butterworth filter on the spatial autocorrelations, spectra and Taylor macro and micro scale estimates both without and with the Nyquist criteria for the spatial sampling, i.e., sampling at cutoff $dx_c = 2dx = 8.555$ mm, as shown in Tables D1-4-1 and D1-4-2 and Figures D1-3 and D1-4. Tables D1-4-1 and D1-4-2 show spatial micro scale summaries obtained by the following two methods: (1) The root of the parabola fitted to three points [r_i, $f(r_i)$] before and after the origin r=0 (method used in the paper). (2) Finding r where $f(r)$ equals the half-peak value [$f(r)$ = 0.5]. The Butterworth filter autocorrelations are like the unfiltered data as is E_{11} with dx, whereas E_{11} with dx_c removes the anomalous behavior for the large wave numbers. The results with the Butterworth filter and dx show larger Taylor macro and micro scales than the temporal analysis, as was the case using the unfiltered data. The micro scale with the Butterworth filter and dx_c as shown in Table 4-1, exhibit anomalous behavior that the micro scale is larger than the macro scale shown in Table 5. This anomaly is due to the coarseness of the spatial resolution affecting the parabola fitting method used in Table 4-1. Table 4-2 shows the r value where $f(r)$ reaches its half-peak value [$f(r)$ = 0.5], detected by linear interpolation. This value is generally used as an index to evaluate the width of the autocorrelation function. The two cases (unfiltered and Butterworth with dx) other than Butterworth with dx_c give results like those of parabola fitting used in the paper. As shown in Figures D1-3 and D1-4, the shapes of $f(r)$ are almost the same, so it is suggesting that the microscale values will also be similar. This new index gives reasonable microscale values. We will use this index for future publications.

We plan on using the Butterworth filtered results for the journal publication of our SNH paper.

Comment 4: Thank you for pointing this out. We fixed this mistake.

Comment 5: The differences in the experiments are because of differences in their measurement volumes, resolutions, and data rates. In general, we expect the 4DPTV to be more accurate than the TPIV. However, since the analysis focuses only on a single point, it may not be providing a complete picture of the strengths and advantages of the two measurements. This study provides a framework for the analysis methods, which will be applied for additional points along a radial line perpendicular to the vortex core at x/L= 0.12 and at points upstream and downstream from x/L = 0.12 along vortex core that would aid evaluation turbulence structure and experimental methods better.

Table D1-4-1: Spatial Micro Scale (Parabola fitting, used in the paper)

Micro scale	Δr[mm]	Three points parabola fitting and finding the root	
		Spatial(symmetric)	Spatial(antisymmetric)
Unfiltered (SNH35th)	4.277	6.85E-03	7.17E-03
Butterworth (fc,145.9Hz) without skip	4.277	7.06E-03	7.43E-03
Butterworth (fc,145.9Hz) with skip	8.555	1.13E-02	1.14E-02

Table D1-4-2: Spatial Micro Scale (Half peak)

Micro scale	Δr [mm]	Finding r where half peak ($f(r) = 0.5$)	
		Spatial(symmetric)	Spatial(antisymmetric)
Unfiltered (SNH35th)	4.277	6.55E-03	7.35E-03
Butterworth (fc,145.9Hz) without skip	4.277	7.00E-03	7.73E-03
Butterworth (fc,145.9Hz) with skip	8.555	7.40E-03	7.93E-03

Table D1-5: Spatial Macro Scale

Macro scale (Λ_f[m] by Simpson)	Δr[mm]	Spatial(symmetric)	Spatial(antisymmetric)
Unfiltered (SNH35th)	4.277	8.67E-03	9.61E-03
Butterworth (fc,145.9Hz) without skip	4.277	9.14E-03	1.00E-02
Butterworth (fc,145.9Hz) with skip	8.555	8.94E-03	1.04E-02

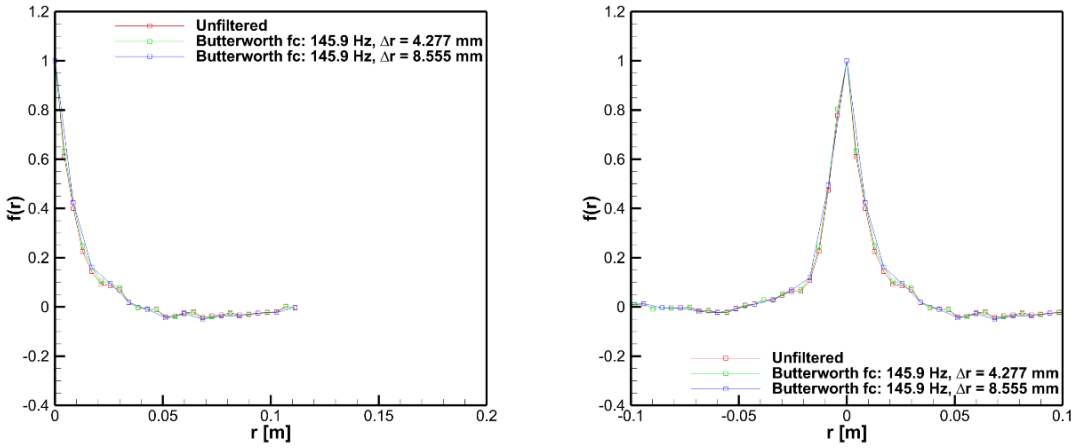

Figure D1-3: Spatial autocorrelation comparison: Symmetric (left) and Antisymmetric (right)

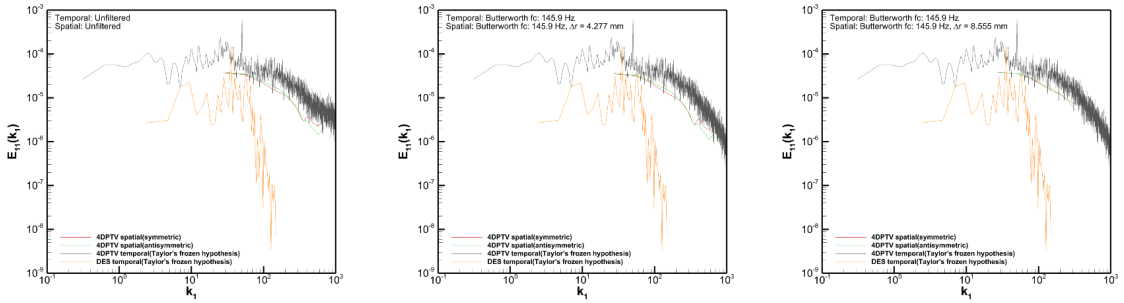

Figure D1-4: E11 comparison original (unfiltered) (left), with Butterworth filter (fc: 145.9Hz, Δr = 4.277 mm) (middle), and with Butterworth filter (fc: 145.9Hz, Δr = 8.555 mm) (right)

Table D1-5: Comparison Macro Scale SNH Paper and corrected values

Parameter	Table 2 ($L = l_0/0.43$)		Corrected%Original
	Original	Corrected	
$\langle U \rangle$ [m/s]	1.255	1.248	0.53%
$\langle u^2 \rangle$ [m^2/s^2]	0.018	0.018	-1.27%
k [m^2/s^2]	0.048	0.048	-0.25%
u_0 [m/s]	0.219	0.219	-0.12%
l_0 [m]	0.025	0.025	0.00%
L [m]	0.058	0.058	0.00%
ε [m^2/s^3]	0.181	0.182	-0.37%
Re_L	10780.2	10793.4	-0.12%

Table D1-6: Comparison Micro Scale SNH Paper and corrected values

Parameter	Table 3 Temporal 4DPTV ($L = l_0/0.43$)		Corrected%Original
	Original	Corrected	
$\langle U \rangle$ [m/s]	1.255	1.248	0.56%
τ_E [s]	3.66E-03	3.72E-03	-1.58%
T [s]	6.05E-03	6.42E-03	-6.11%
λ_f [m]	4.59E-03	4.64E-03	-1.01%
Λ_f [m]	7.59E-03	8.01E-03	-5.52%
R_λ	4.92E+02	4.97E+02	-1.14%
ε [m^2/s^3]	5.38E-02	5.28E-02	1.76%
η [m]	7.44E-05	7.48E-05	-0.44%

The DES predictions predict the flow qualitatively well, but it is found to be more diffusive and dissipative than the experiment. One would expect to resolve these limitations by using even finer grids. However, considering our previous DES studies and in particular the DES submission in NATO-AVT 253 wherein the grids were sufficiently fine to resolve the Taylor microscale; fine grid simulations accentuate the limitations of the DES models. For example,

(1) they fail to preserve URANS in boundary layer on very fine grids resulting in modeled stress depletion and grid induced separation.
(2) they lack dissipation in the LES region because of explicit LES modeling; and
(3) on fine grids with 95% resolved turbulence and boundary layer resolved using URANS, they underpredict TKE and vorticity strength during vortex progression (Bhushan et al. 2019).

Nonetheless as our study has shown they provide useful information augmenting the measurements, e.g., concerning the spiral vortex breakdown and helical mode instability.

Improved hybrid RANS/LES models are needed that can preserve URANS in the boundary layer, as well as address the modeled stress depletion issue by enhancing resolved turbulence at the RANS/LES interface. The underprediction of TKE in the vortex core in the well resolved LES region could be partly related to the under resolved turbulence at the core or partly because of numerical dissipation. Thus, higher order numerical schemes, such as 4th order schemes, should be investigated. The dynamic hybrid RANS/LES model (Bhushan and Walters, 2012) addresses those challenges, which has been validated for a wide range of engineering applications, including addressing grid sensitivity and modeled stress depletion issues (Zope et al., 2021).

REFERENCES

Bendat, J. S., and A. G. Piersol (1986), Random Data, 2nd ed., 566 pp., John Wiley, New York

Bhushan, S., and Walters, D.K. (2012). "A dynamic hybrid RANS/LES modeling framework," Physics of Fluids, 24, 015103.

Kang HS, Chester S, Meneveau C (2003). Decaying Turbulence in an Active-Grid-Generated Flow and Comparisons with Large-Eddy Simulation. Journal of Fluid Mechanics 480: 129-160.

Sanada, Y., Starman, Z., Bhushan, S., and Stern, F., "Four-dimensional particle tracking velocimetry measurements of unsteady 3D vortex onset and progress for 5415 straight ahead, static drift and pure

sway," Physics of Fluids, Vol. 35(10), 2023, 105125. https://doi.org/10.1063/5.0165658.

Frederick Stern, Yugo Sanada, Zachary Starman, Shanti Bhushan, Christian Milano, "4DPTV Measurements and DES of the Turbulence Structure and Vortex-Vortex Interaction for 5415 Sonar Dome Vortices," 35th Symposium on Naval Hydrodynamics, Nantes, France, 7 July - 12 July 2024.

Zope, A, Schemmel, A, Wang, X, Bhushan, S, Singh, P, and Luke, E, "Assessment of Predictive Capability of Hybrid RANS/LES Turbulence Models for Thermofluid Applications," ASME 2021 Fluids Engineering Division Summer Meeting.

DISCUSSION 2 (D2)

Philippe Spalart, The Boeing Company (retired)

I am new to Naval Hydrodynamics. In the last few years for Aerodynamics, I have been pleased by the excellent collaboration between experimental and CFD experts, with the turbulence-modeling experts regularly consulted; here, the experts are even members of one team.

1. The ambition level is very high. The comparisons are searching and do not shy from detailing differences between the datasets. As an example, k in Table 2 takes the values 0.048, 0.030, and 0.014, and the dissipation numbers differ by fully a factor of 15. This is very concerning. In fact, some of the findings are excessively negative in my opinion.

2. It is a sign of the times and lessons learned that no RANS results are presented, even with vortex corrections. I agree that the present flow is complex enough to justify a turbulence-resolving approach. RANS results would have value to me but would inflate the paper, especially if several model versions were involved.

3. It is also excellent that two experimental techniques are used, so that the report does not have the tone of a straightforward "experiment against CFD" exercise. This single-test situation has been an issue in some workshops in Aerodynamics. I expect the 2024 SNH Symposium to, in addition, contain a variety of CFD datasets.

4. The statement that DES returned two-dimensional turbulence is too sweeping, considering that only one point is considered. I would also see much value in an instantaneous flow visualization that displays convincing LES content in that region, to rule out an ambiguous "RANS or LES?" situation there. Figure 7 shows that the DES is severely under-resolved.

5. Before I move into low-level comments, let me express my fond hope that the distance between all our sources of knowledge will shrink fairly rapidly.

6. There is much room for improvement in terms of completeness. I believe the quantities shown in Fig. 1 are not described, and also that the point where results in Figs. 11 and 12 were taken is not known. The differences are strong. Is it possible the data are from the same (x,y,z) point, but it is not in the same position relative to a vortex? Remember Fig. 2. I also wonder how the DES dissipation was calculated.

7. As always, I must object to distinctions between the three normal Reynolds stresses and the other three. Use a different orientation of the (x,y,z) axes, and the two categories communicate. Of course, in the principal axes, there are only normal stresses. Only the trace of the matrix has its own meaning.

8. I note as always that the Q criterion, which was created to bring out vortices and not shear layers, brings out boundary layers on convex surfaces, which causes confusion. In due time, I'd like to see the effect of a minor modification I have concocted.

9. I did not expect Gaussian or bell distributions for Q, since at the edge of a normal vortex, Q crosses 0 linearly, becomes negative, and gradually returns to 0.

10. Instantaneous figures from the DES would be very valuable; it is essential to see where the solution starts having "LES Content." It is possible that some of the vortex smearing see in Fig. 2c took place before the switch to LES.

11. Are the points in Fig. 10a from DES? Or are they from Muthu's simulation of another flow, and should be ignored?

12. Personally, I would report non-dimensional quantities in Tables 1 and 2, and others. Many figures also mix dimensional and non-dimensional quantities.

13. Table 5 has a distracting feature. An eigenvector can be switched in sign. Thus, the agreement between TPIV and DES for x_R2 is actually fairly good. Somehow, the x_R3 row was "lucky."

AUTHOR'S REPLY

Thank you and we appreciate all of your comments, which are addressed below.

Comment 1: We would like to point out that the evaluation of turbulent autocorrelations, spectra, and Taylor and other macro and micro scales in our field especially for practical geometries are seldom if ever done, which is not to excuse the aforementioned differences but rather to make the point that this is the state-of-the-art and sets the bar for future improvements. In our response to the Charles Meneveau discussion item #2 we have fully explored and explained the reasons for these differences and provided the following hypothesis: to achieve proper resolution of the energy containing range macro scales, turbulence anisotropy and organized oscillations it is necessary to simultaneously resolve both the temporal and spatial Taylor micro (λ_f) and macro (Λ_f) scales in experiments and/or simulations. We hope to convince our sponsors to support future experiments and/or simulations to enable us to provide proof of this hypothesis.

Comment 2: In our previous study using the TPIV data for this flow, i.e., AVT-253, we had already assessed the RANS capability and therefore felt no need to include herein; especially as we have not observed new developments in RANS capabilities for our application.

Comment 3: Thank you.

Comment 4: Although our analysis is just for one point at the vortex core, we believe that the results are representative of the turbulence behavior of the vortex region at this location. Figure D2-1 shows the (a) LES and URANS region, (b) instantaneous velocity and (c) mean velocity components at x/L = 0.12 and highlights the degree to which the LES modeling was activated. Clearly, DES predicts significantly under-resolved turbulence even though the grid is fine enough to activate LES. Note that AVT-253 analysis for this flow did include a section on hybrid-RANS/LES (HRLES) Quality and Regions, which included more extensive analysis of our and other results.

As stated in our paper: "The present DES was obtained many years ago and herein the results on the finest grids are not used. Nonetheless, in consideration of its performance compared to the other methods, the present results are representative of current state-of-the-art methods, and they are an indication of the directions needed for improvements of HRLES methods."

Comment 5: We also would like to see improvements both in our experimental and HRLES capabilities.

Comment 6: Our precursory PoF paper (https://doi.org/10.1063/5.0165658) provides extensive discussion of the quantities shown in Fig. 1. All our analysis is at the mean vortex core position for SDVP at x/L=.12 as estimated by each of our analysis methods (see discussion Table 1).

In Table 2, dissipation is computed using the equation: $\varepsilon = u_0^3/L$ for both experiments and CFD. Footnote 1 provides details of the estimate. Yes, we agree that in CFD we can get RANS modeled dissipation from the ω equation. Since there is no explicit LES, we can directly estimate the dissipation by the LES modeling. Considering that resolved turbulence is minimal at this location (see Figure D2-2), the modeled dissipation calculation should be significantly larger than the LES modeling component. These estimates show significantly large dissipation $\varepsilon \sim 1\ m^2/s^3$. A significantly large ε could be the source of the modeling issue.

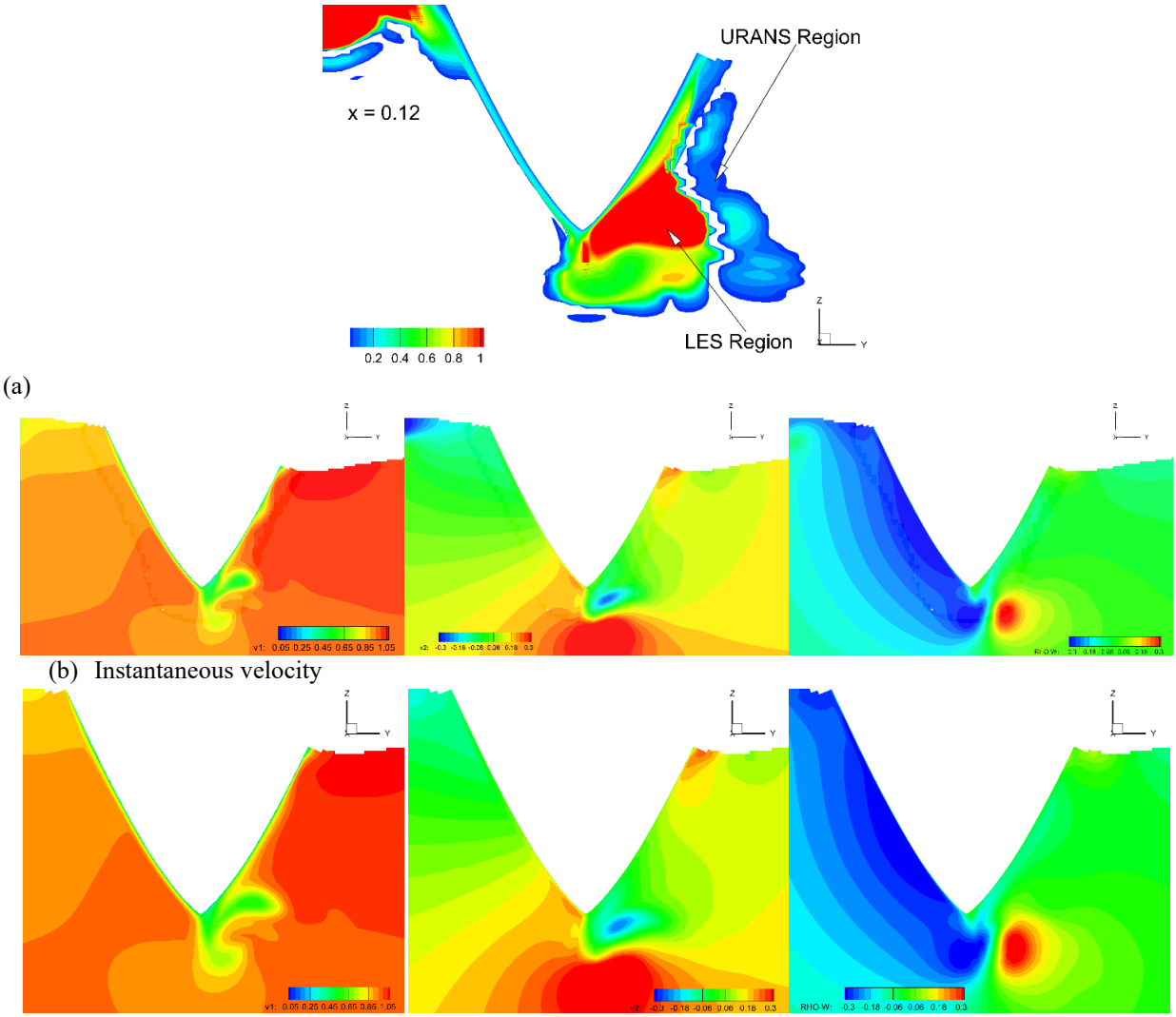

Figure D2-1: (a) LES and URANS region, (b) instantaneous velocity and (c) mean velocity components.

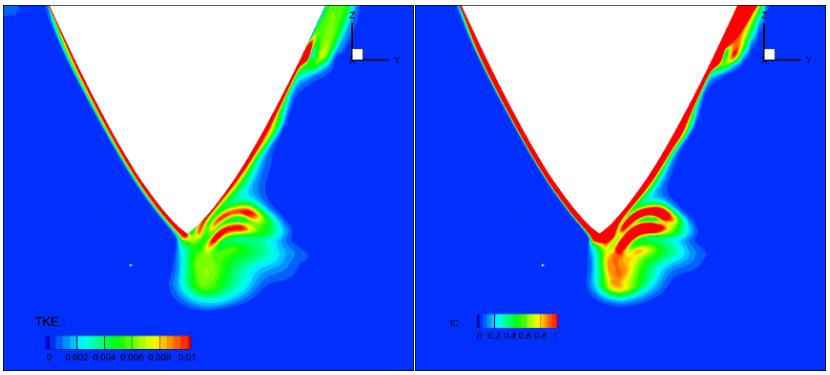

Figure D2-2: Modeled TKE and dissipation at x/L = 0.12.

An order of magnitude lower ε in CFD compared to experiments as shown in Table 2 is mostly due to the lower TKE (and u_0) predictions.

Comment 7: We agree that Reynolds stresses in any reference system can be transformed into their representation in principal axes, where only the normal stresses are non-zero. We believed it would be valuable to present the Reynolds stress tensor components both as directly obtained from the experiments/CFD (Figures 11 and 12) and in the principal axes reference frame (Figures 13 and 14).

Comment 8: Please provide us your Q modification and we will investigate it in our future research.

Comment 9: We will investigate that in a normal vortex, Q crosses 0 linearly, becomes negative, and gradually returns to 0; and adjust our analysis, discussion, and conclusions as needed.

Comment 10: See Figure D2-1 and the AVT-253 Final Report.

Comment 11: They are from a different study and have been removed in the final version of our paper.

Comment 12: We found it useful in assessing our resolution capabilities to use dimensional "real" values while at the same time found it also useful to use non dimensional values.

Comment 13: We agree that the eigenvectors can be switched in sign. Our intention in presenting the eigenvector components in Table 5 was to highlight the directions of the principal axes of the Reynolds stress ellipsoid. However, we believe that a more accurate assessment of the agreement between 4DPTV, TPIV, and DES is given by the angles between the eigenvectors (the RS ellipsoid principal axes) and the mean velocity/vorticity, as shown in Table 6.